Near-Surface Turbulence in the Presence of Breaking Waves

JOHANNES R. GEMMRICH

Institute of Ocean Sciences, Sidney, British Columbia, Canada

DAVID M. FARMER

Institute of Ocean Sciences, Sidney, British Columbia, Canada, and University of Rhode Island, Narragansett, Rhode Island

(Manuscript received 17 March 2003, in final form 27 October 2003)

ABSTRACT

Observations with a three-axis pulse-to-pulse coherent acoustic Doppler profiler and acoustic resonators reveal the turbulence and bubble field beneath breaking waves in the open ocean at wind speeds up to 14 m s^{-1}. About 55%–80% of velocity wavenumber spectra, calculated with Hilbert spectral analysis based on empirical mode decomposition, are consistent with an inertial subrange. Time series of turbulent kinetic energy dissipation at approximately 1 m beneath the free surface and 1-Hz sampling rate are obtained. High turbulence levels with dissipation rates more than four orders larger than the background dissipation are linked to wave breaking. Initial dissipation levels beneath breaking waves yield the Hinze scale of the maximum bubble size $a_H \cong 2 \times 10^{-3}$ m. Turbulence induced by discrete breaking events was observed to decay as $\varepsilon \propto t^n$, where $n = -4.3$ is close to the theoretical value for isotropic turbulence ($-17/4$). In the crest region above the mean waterline, dissipation increases as $\varepsilon(z) \propto z^{2.3}$. Depth-integrated dissipation in the crest region is more than 2 times the depth-integrated dissipation in the trough region. Adjusting the surface definition in common turbulence models to reflect the observed dissipation profile improves the agreement between modeled and observed dissipation. There is some evidence that turbulent dissipation increases above the background level prior to the air entrainment. The magnitude and occurrence of the prebreaking turbulence are consistent with wave–turbulence interaction in a rotational wave field.

1. Introduction

At moderate to high wind speed the momentum transfer from wind to ocean currents passes through the wave field via wave breaking. The breaking of surface waves is responsible for the dissipation of wave energy. Thus, wave breaking is believed to be a source of enhanced turbulent kinetic energy (TKE) levels in the near-surface layer and to play an important role in upper-ocean processes. Vertical transport of heat, gases, and particles in the near-surface zone depend on turbulence; increased turbulence intensity leads to enhanced air–sea exchange processes. Comprehensive overviews of the role of wave-induced turbulence in upper-ocean dynamics and air–sea exchange processes are given by Thorpe (1995), Melville (1996), and Duncan (2001). Recent measurements with an autonomous vehicle confirm that wave breaking dominates the near-surface turbulence and that Langmuir circulation and shear-induced eddies are important processes below the depth of a few times the wave height (Thorpe et al. 2003). Wave tank experiments have identified wave-breaking-induced vortices that are persistent for tens of wave periods (Melville et al. 2002). In the field, the vertical momentum transport associated with these vortices is expected to be small compared to incoherent turbulence and difficult to identify (Melville et al. 2002). The focus of this article is turbulence generated by actively breaking waves.

The ocean surface is a complex environment with a wide range of relevant scales. Direct measurement of the velocity field is a first step to its description. In addition to the overall wave orbital motion, a useful parameter characterizing the turbulence field is the dissipation rate of turbulent kinetic energy ε. There are three different approaches taken to estimate dissipation ε. (i) Microstructure profilers measure the turbulent shear variance, which is proportional to ε (Soloviev et al. 1988; Anis and Moum 1992). Lueck et al. (2002) review the historical development of velocity microstructure profilers. Operated in a rising mode these instruments yield dissipation profiles close to the surface. However, the temporal resolution at any given depth is very intermittent. (ii) At sufficiently high wavenumber and in the steady state, the statistical structure of turbulence depends only upon ε (Hinze 1975). Therefore, the dissipation rate may be inferred from velocity mea-

Corresponding author address: J. Gemmrich, Institute of Ocean Sciences, P.O. Box 6000, Sidney, BC V8L 4B2, Canada.
E-mail: gemmrich@uvic.ca

surements at a single point. However, these measurements require conversion from frequency space into wavenumber space via Taylor's frozen turbulence hypothesis. Measurements from a fixed mooring (Agrawal et al. 1992; Terray et al. 1996) rely on the extension of Taylor's hypothesis for unsteady advection (Lumley and Terray 1983). Towed or vessel-mounted velocity measurements (Stewart and Grant 1962; Drennan et al. 1996; Soloviev et al. 1999) avoid the additional uncertainties associated with unsteady advection. (iii) Here we use direct spatial measurements obtained with an acoustic Doppler profiler (Veron and Melville 1999) and no transformation of a temporal signal into a spatial signal is required.

Although previous studies provide strong evidence that turbulence in the ocean surface layer is largely enhanced due to wave breaking (Agrawal et al. 1992; Terray et al. 1996; Soloviev and Lukas 2003), the direct link between breaking and enhanced dissipation remains to be examined. We describe observations of turbulence and the bubble field 1 m below the free surface at wind speeds >10 m s^{-1} with frequent wave breaking and examine the relation between wave breaking and subsurface turbulence.

2. Measurement approach

Measurements yielding dissipation estimates in the near-surface layer are difficult to make. In the past it has been necessary to average over a few wave periods to several minutes to achieve stable estimates (Terray et al. 1996). However, if we are to directly relate individual breaking waves to turbulence, we need turbulence measurements with a resolution comparable to that of the wave breaking itself and to combine these measurements with independent observations of wave breaking. Breaking occurs at the wave crest and typically covers a few tenths of a wavelength (Wu 1992). Hence, it will pass a stationary point in about 1 s, requiring comparable temporal resolution in the measurement.

Observations of the turbulent velocity and bubble field were taken during 24 September–10 October 2000 as part of the Fluxes, Air–sea Interaction and Remote Sensing (FAIRS) experiment aboard the research platform (R/P) *Floating Instrument Platform* (*FLIP*) in the open ocean 150 km offshore of Monterey, California. A 0.9 m $\times$ 1.2 m surface float, tethered to the starboard boom, supported three orthogonal 2-MHz pulse-to-pulse coherent acoustic Doppler sonars (Dopbeam, Sontek) and two acoustical resonators (Farmer et al. 1998) as well as an environmental package, monitoring water temperature, salinity, and float tilt and heading (Fig. 1). The float was suspended from a mast about 7 m in the orthogonal direction to the wind and 20 m downwind from the hull so as to avoid wake and other contamination effects of the vessel. The float supported the sensors at nearly constant depth beneath the surface with

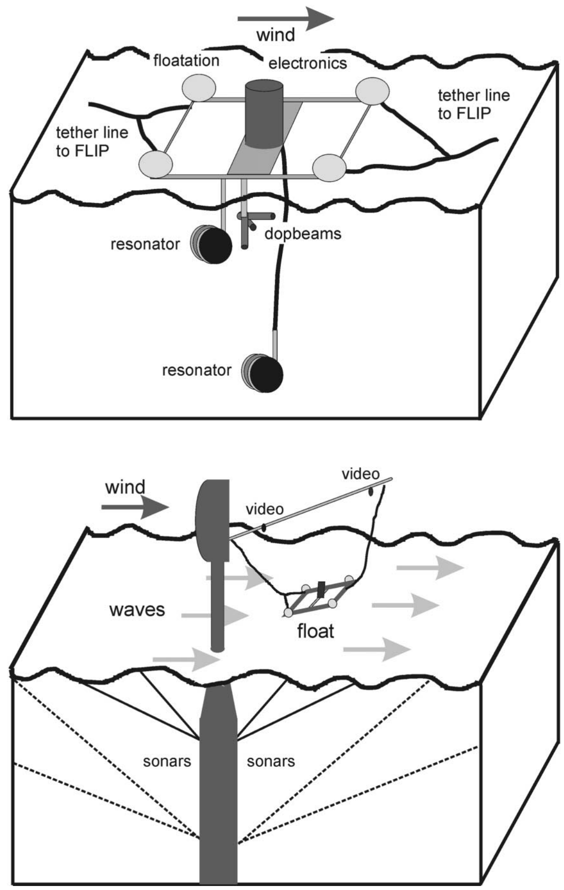

FIG. 1. (top) Sketch of the 1.2 m $\times$ 0.9 m surface-following float. The shallow resonator and the head of the vertical Dopbeam are at approximately 1-m depth; the deeper resonator is at 2.5 m. (bottom) Sketch of the deployment setup. The float was tethered to the starboard boom of R/P *FLIP*, approximately 20 m from *FLIP*'s hull. The design of *FLIP* and the offset of the float position relative to the wind direction minimize flow distribution at the float.

minimal flow disturbance at the measurement location. Visual observations showed that this design allowed the instrument to ride on the waves without avoiding steep waves or breaking wave crests. During the passage of a wave, video observations showed that the float turned into the wave direction and followed the free surface, moving up to 2 m horizontally back and forth.

The Dopbeams acquired velocity profiles of 0.72-m length, in a path that begins 0.14 m ahead of the sensor head, and with 6×10^{-3} m radial bin size (Fig. 2a). The diameter of the sonar transducer is 25×10^{-3} m and the beamspread half-angle is 1.2°. Near-field effects are limited to the first 0.2 m (from the sensor head) and the maximum beamspread is 35×10^{-3} m at the far range of the profile [see Zedel et al. (1996) for details]. The R/P *FLIP* drifted freely, orienting itself in the wind direction. Therefore, the two horizontal sonars at 0.6-m depth pointed nominally in the downwind (u) and crosswind (v) direction. The third sonar pointed vertically downward ($-w$) with the sensor head located at

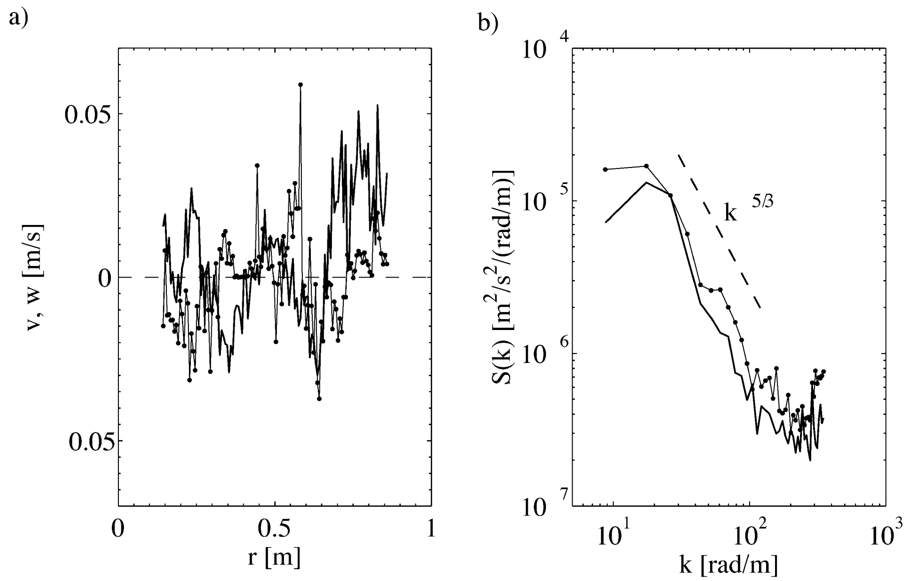

FIG. 2. (a) Sample velocity profiles in cross-wind (solid) and vertical (dotted line) directions as function of range r. (b) One-second averaged wavenumber spectra from cross-wind (solid) and vertical (dotted line) velocity profiles. Dashed line depicts slope of inertial subrange.

0.7-m depth. The three velocity profiles (u, v, w) were not quite collocated. The sampling frequency was 20 Hz. In the following, we adopt a right-handed Cartesian coordinate system and define the vertical axis positive upwards.

The free-flooding resonators are used to determine the size distribution of microbubbles, generated by breaking waves. The resonators resolve bubble sizes of approximately 20–200 μm at 2.2-Hz sampling frequency. Integration of the bubble size spectra yields the mean air fraction γ over this size range within the resonator cavity. Resolved air fractions are $10^{-8} \leq \gamma \leq 10^{-4}$. The instrument is not suited for high air fractions, but for $\gamma < 10^{-5}$ it is well centered to resolve the relevant bubble size distributions. One unit was mounted approximately 0.2 m to the side of the downward-looking sonar. The second resonator was suspended from a wire cable at 2.6-m depth.

Simultaneous video recordings were made with two cameras mounted on R/P *FLIP*. The field of view of both cameras included the float, and recordings are used to verify the occurrence and estimate the size of breaking waves at the float. A set of eight 100-kHz side-scan sonars, mounted on *FLIP*'s hull at depth ranging from 15 to 91.5 m, was used to estimate the directional wave field (Trevorrow 1994) as well as the surface drift speed.

a. Dissipation of turbulent kinetic energy

Our goal is to examine the relation between wave breaking and energy dissipation ε. According to Kolmogorov's hypothesis, there exists an inertial subrange where the three-dimensional wavenumber spectrum of a high Reynolds number flow has a universal form that depends only on the energy dissipation. For isotropic turbulence, the one-dimensional wavenumber spectrum $S(k)$ takes the following form (Hinze 1975):

$$S(k) = A\frac{18}{55}\varepsilon^{2/3}k^{-5/3}, \tag{1}$$

where k is the wavenumber and $A = 1.5$ is a universal constant.

This simple relationship between energy dissipation and wavenumber spectra (1) is the basis for estimating ε. The wavenumber spectrum is calculated for each velocity profile using the Hilbert spectral analysis. The velocity profile represents a broadband signal that is decomposed into several narrowband intrinsic mode functions (Huang et al. 1998, 1999). Application of the Hilbert transform on these intrinsic mode functions yields the local wavenumbers and amplitudes as a function of profiling range. The Hilbert transform of the function $g(x)$ is defined by

$$H(x) = \frac{1}{\pi}P\int_{-\infty}^{\infty}\frac{g(t)}{(x - t)}\,dt. \tag{2}$$

Because of a possible singularity at $x = t$, the integral has to be taken as a Cauchy principal value P. The original function and its Hilbert transform form the analytical function $Z(x) = g(x) + iH(x)$. The amplitude and phase of this signal are

$$a(x) = [g(x)^2 + H(x)^2]^{1/2} \quad \text{and} \quad \theta(x) = \arctan\left[\frac{H(x)}{g(x)}\right], \tag{3}$$

respectively. The local wavenumber is

$$k(x) = \frac{d\theta(x)}{dx}. \quad (4)$$

Amplitudes and wavenumbers are calculated from each intrinsic mode function. The wavenumber spectrum is obtained by integration of the squared amplitude along the entire profile. The profiling range (0.72 m) and the coarsest spatial resolution (35×10^{-3} m) determine the wavenumber resolution 9 rad m^{-1} $< k <$ 180 rad m^{-1}. Utilizing the entire velocity profile requires that turbulent properties are uniform along the complete path. To check the validity of this assumption, we split the velocity profile into near field (0–0.36 m) and far field (0.36–0.72 m) prior to calculating the wavenumber spectra, thereby increasing the low wavenumber cutoff to $k > 18$ rad m^{-1} as well as decreasing the degrees of freedom in the spectral analysis. Although computationally more elaborate than the commonly used Fourier spectral analysis, the use of the Hilbert spectral method based on intrinsic mode functions is more appropriate for nonstationary and short data records than the Fourier method, which is strictly limited to linear, stationary data.

The characteristic time scale associated with the inertial subrange $\tau_t = (\nu/\varepsilon)^{1/2}$ depends on the kinematic viscosity ν and dissipation (Hinze 1975). For typical dissipation values encountered in the near-surface layer, this time scale ranges from $O(10^{-2}$ s) to $O(1$ s). Therefore individual spectra having a 20-Hz sampling rate are averaged to obtain robust spectra at 1-s intervals (Fig. 2b). These averaged spectra are checked for the existence of a $k^{-5/3}$ slope, indicative of an inertial subrange. The inertial subrange concept represents an idealized case of isotropic, steady-state turbulence, which is not always applicable in the ocean surface layer. The intermittency of the turbulence generation, advection of turbulence by the wave orbital motion, the proximity of the surface, and the presence of dense bubble clouds will distort this idealized spectral shape at certain times. For the evaluation of the spectral shape, we use maximum likelihood spectral fitting (Ruddick et al. 2000) and allow for a variable wavenumber range in our calculation of the slope. The instrumental noise spectrum required for the maximum likelihood fitting has been determined from data recorded in calm water off the dock at the Institute of Ocean Sciences. Dissipation values are calculated according to (1) from averaged spectra that are consistent with the inertial subrange. For the full range profiles about 50%–75% of the spectra have properties consistent with an inertial subrange. Using only one-half of the profile, this percentage drops to 45%–70% with no significant difference between the near field and far field. However, between 65% and 90% of the averaged spectra are consistent with an inertial subrange in at least one part of the path. The intermittent occurrence of an inertial subrange appears random (Fig. 3). Data records with the highest percentage of resolved inertial subranges occur mainly at moderate wind speeds. However, we did not find any significant correlation between the percentage of resolved subranges and environmental parameters like wind speed or wave steepness that would hold for all deployments. In the following, dissipation estimates are the average of estimates based on the near field, far field, and entire profile. No dissipation estimates are obtained in cases in which none of the three spectra show an inertial subrange.

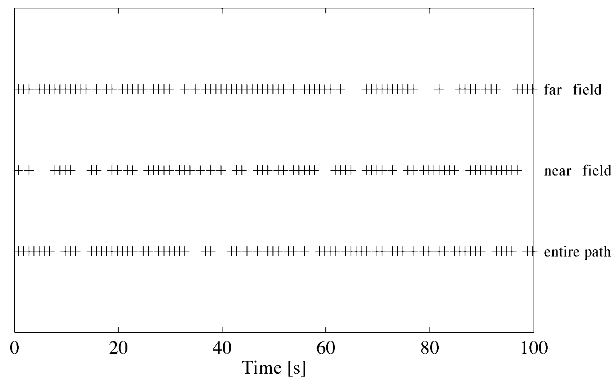

FIG. 3. Time series of occurrence of inertial subranges at wind speed 11 m s^{-1} (0000 UTC 10 Oct 2000). Each cross indicates that the 1-s-averaged wavenumber spectra are consistent with the properties of an inertial subrange.

A major challenge of oceanic turbulent velocity measurements is the separation of wave-induced motion and turbulence. Orbital velocities of the dominant waves are $O(1$ m s$^{-1})$ whereas typical turbulent velocities are $O(10^{-2}$ m s$^{-1})$. The magnitude of the orbital motion is a strong function of distance to the surface. At a distance z below the still waterline, the vertical velocity of a linear wave varies as $w(z) = a\omega e^{-k|z|}$, where a is the amplitude and ω is the frequency of an individual wave component. The largest scale resolved in our velocity profile is $k = 9$ rad m^{-1} and the wave orbital motion at this wavelength is $O(10^{-4})$ of its surface value, which is negligible. Larger waves, which are associated with significant orbital motion at the profile depth, result in a constant velocity offset, which does not affect the spectral level of the inertial subrange (see the appendix). Therefore, a separation of turbulent and wave-induced velocities is not required for our instrumentation setup.

b. Surface elevation

An estimate of the local surface elevation may be obtained from the horizontal velocity record. The wave orbital velocity is the combination of the downwind u and cross-wind υ velocity component $c = u \pm \upsilon$, where the sign depends on the orientation of the float relative to the wave. The surface elevation is

$$\eta = \int H(c)\, dt = \eta_x \pm \eta_y, \quad (5)$$

where the symbol H represents the Hilbert transform and $\eta_x = -\int H(-u)\,dt$, $\eta_y = \int H(v)\,dt$. In practice, the velocity records are the mean value of the first three velocity bins and are high-pass filtered with a cutoff at 0.04 Hz prior to applying the Hilbert transform. Generally, the total surface elevation is dominated by the downwind component, $\eta_x \geq 100\eta_y$, and η_y represents only a small correction. Visual observations confirmed that the float is turning into the waves such that the downwind component is nearly always parallel to the wave propagation. However, the float drifts up to 2 m back and forth from the wave motion. This motion can be tracked on the video recordings, and for specific datasets the error due to the instrument motion can be removed from the time series. If the time series is uncorrected, the recorded velocity is reduced and (5) yields the correct phase of the waves but underestimates the amplitude.

The surface elevation was monitored with a sonic range finder mounted on the same instrumentation boom (A. Jessup, Applied Physics Laboratory, University of Washington, 2000, personal communication). At ranges that are far in comparison with the depth, the side-scan sonars mounted on *FLIP*'s hull yield nearly horizontal surface velocities. Integration of the velocity record at a single range bin, according to (5), provides a further estimate of the surface elevation time series. The shape of the 1D power spectra obtained from the float data is in good agreement with wave spectra obtained with these additional measurements; in particular all three methods yield the same peak periods. However, in the absence of corrections for the float motion mentioned above, the significant wave height based on the float data is underestimated by about 25% relative to the other two types of independent measurements. The float motion can be tracked on the video images and this information is used to correct the wave orbital motion recorded relative to the float. While full corrections for float motions are carried out for detailed datasets, for longer time series a simple scale correction is applied:

$$\eta_{\text{true}} = S_\eta \eta, \tag{6}$$

where the scaling factor $S_\eta = H_s/4\sigma(\eta)$; H_s is the significant wave height obtained from independent measurements and $\sigma(\eta)$ is the standard deviation of the surface elevation time series (5).

3. Observations

The FAIRS experiment included three deployments of our float during periods of frequent wave breaking and wind speed up to 15 m s^{-1}. The three deployments cover similar wind speeds but varying degrees of wave development (Fig. 4). Significant wave height H_s and peak period τ_p are based on the side-scanning sonars and are in good agreement with the acoustic range finder data. The wind stress estimates (J. Edson, Woods Hole Oceanographic Institution, 2000, personal communication) are obtained by eddy correlation method.

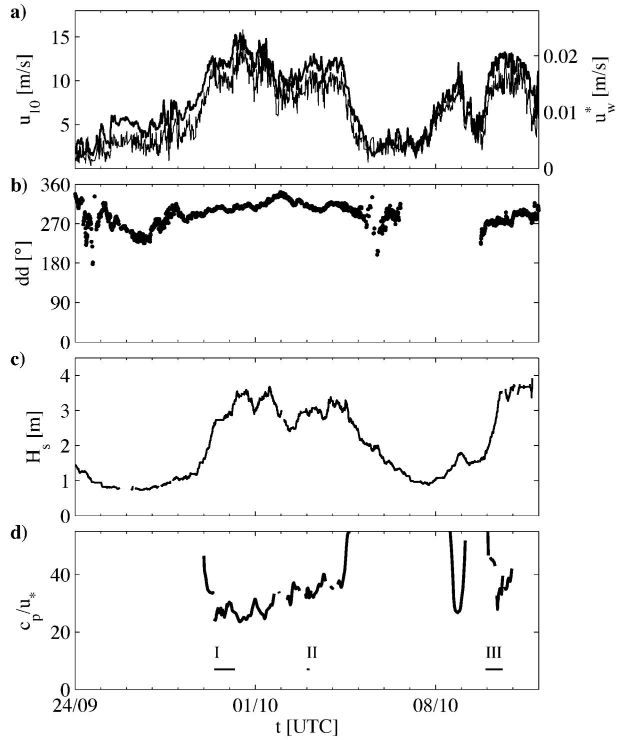

FIG. 4. Environmental conditions during the entire experiment. Individual deployments discussed in this report are indicated in the bottom panel. (a) Wind speed u_{10} at 10 m (thick) and friction velocity in water u_w^*, (b) wind direction dd, (c) significant wave height H_s, and (d) wave age c_p/u_*.

Deployment I, 0950 UTC 29 September to 0510 UTC 30 September 2000, covers the end of a period of increasing wind speed. Throughout the beginning of the deployment the wind speed u_{10} stayed constant at nearly 12 m s^{-1} and increased to 15 m s^{-1} within the last two hours of the deployment with a steady direction from WNW, creating unlimited fetch conditions. The significant wave height H_s increased from 2.2 to 3.5 m. The waves were close to fully developed at wave ages $c_p/u^* \approx 25$, where c_p is the phase speed of the dominant waves and u^* is the friction velocity in air. No turbulence data were recorded at 1730–2250 UTC.

Deployment II, 2355 UTC 2 October–0228 UTC 3 October, occurred after three days of sustained wind speed $u_{10} > 10$ m s^{-1} with well-developed wind waves. The wind speed was $u_{10} \approx 12$ m s^{-1} and wind direction was WNW.

The third deployment, 2240 UTC 9 October–1430 UTC 10 October, covered a rapid increase of wind speed from <5 to ≈12 m s^{-1}. The wind direction stayed constant at 270°, resulting in unlimited fetch. The significant wave height increased from <2 to >4 m and the wave age increased from $c_p/u^* \approx 20$ to $c_p/u^* \approx 40$. No turbulence data were recorded at 0511–0926 UTC. Be-

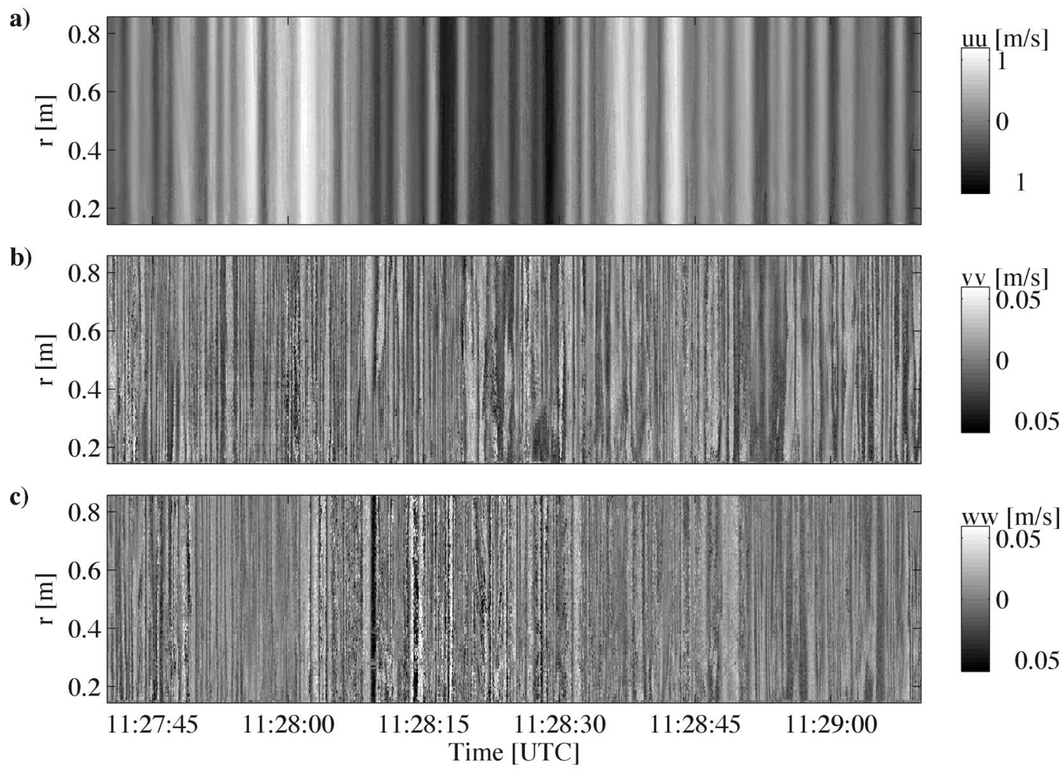

FIG. 5. Segment of velocity field during deployment I. Range r is measured from the head of the Dopbeams in the (a) downwind, (b) cross-wind, and (c) vertical direction, Note: scale of downwind velocity is 20 times that in (b) and (c).

tween 0230 and 0400 UTC data were collected only intermittently.

a. Velocity and dissipation measurements

An example of the observed velocity field is given in Fig. 5. As expected, the strongest velocities are observed in the downwind direction, with magnitudes >1 m s^{-1}, dominated by the wave orbital motion. The maximum cross-wind and vertical velocities are more than one order of magnitude smaller than the downwind component. This is expected for the vertical component (appendix), however not in the nominal cross-wind direction in a directional wave field. The tethering of the float allowed it to be advected sideways and also to turn into waves propagating in different directions. Both float motions would tend to greatly reduce cross-wind orbital motions from the recording. Visual observations and the video recording confirmed the combination of this float behavior. Furthermore, the vertical sonar and the sonar oriented in the cross-wind direction are not affected by the wake of the float and are used to estimate dissipation rates. Several bursts of rapid velocity fluctuations lasting up to 20 s are recorded at both sensors. Generally, the vertical and cross-wind sonar show the same pattern of alternating quiescent and energetic periods.

The dissipation varies over four orders of magnitude within tens of seconds, with no simple dependence on wind speed (Fig. 6). The lowest dissipation rates throughout all three deployments are $O(5 \times 10^{-6}$ m^2 s$^{-3})$ and peak dissipation reaches 10^{-1} m^2 s^{-3}. Possibly due to a lack of scatterers (mainly bubbles), no reliable velocity data could be obtained during low wind speed periods; therefore, no estimates of dissipation in these calm conditions are available. Generally, there is a good correlation between high dissipation rates and the occurrence of breaking waves (Fig. 6). As mentioned in section 2, not all velocity spectra obtained from our data are consistent with an inertial subrange; consequently, the dissipation time series are irregularly spaced. Generally, there is good agreement within the dissipation rates based on the cross-wind and the vertical sonars. However, the horizontal sonar shows a slightly higher rate of unresolved dissipation measurements, which may be linked to the different sensor depth. Particularly within dense bubble clouds the turbulent velocity field cannot be monitored, resulting in a higher dropout rate at the shallower, horizontal sensor during periods of higher wind speed. Dissipation estimates in the subsequent analysis are based on the vertical velocity profiles.

Oceanic turbulence is expected to have a lognormal distribution (Oakey 1985) and may be described by its mean and standard deviation. Taking deployment I as representative of our open-ocean measurements we find

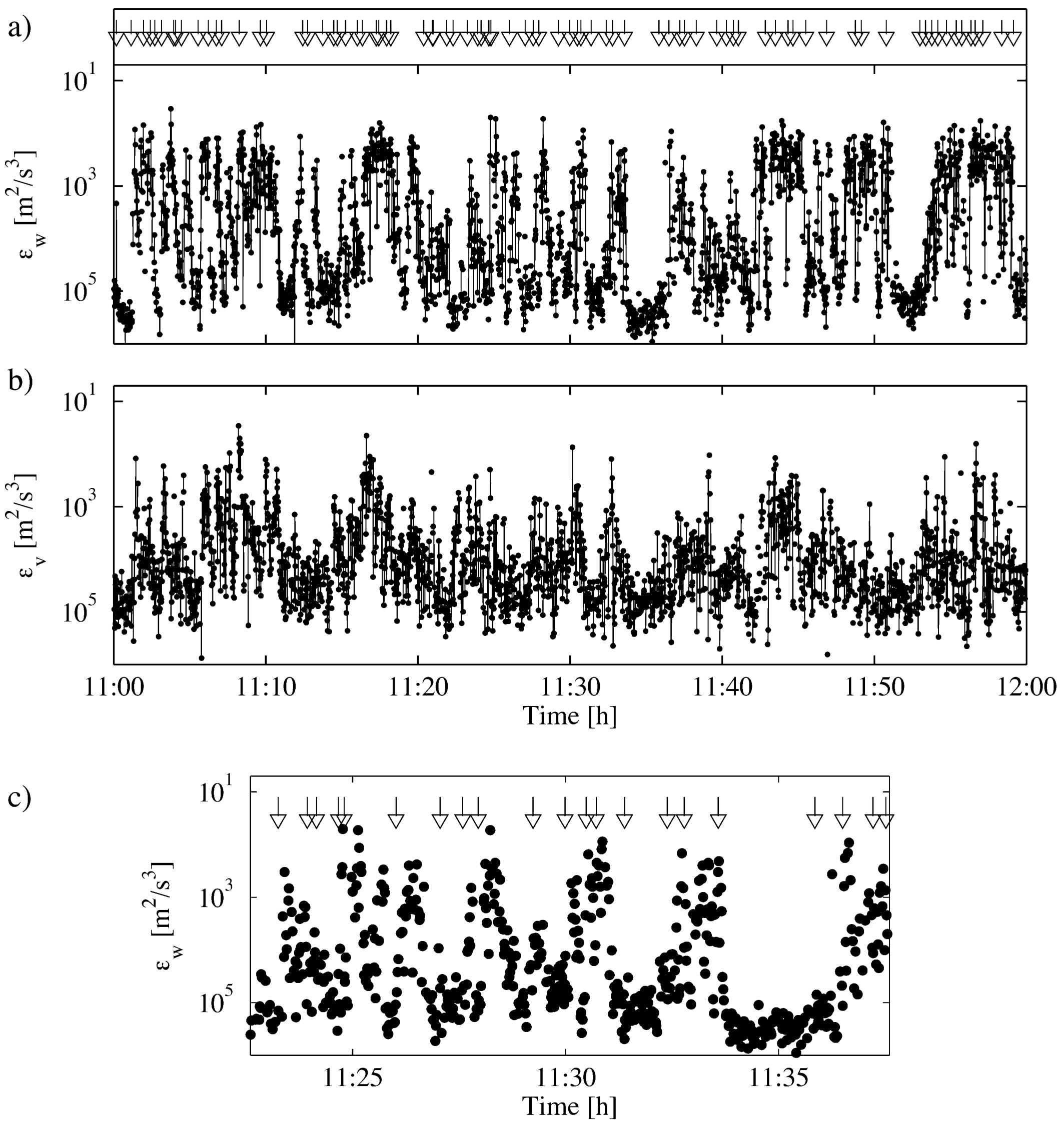

FIG. 6. Segment of dissipation time series for deployment I. Dissipation rates ε are obtained from (a) downward-looking sonars and (b) sonars oriented in the cross-wind direction. (c) Shorter section of (a). Arrows mark occurrence of whitecaps passing the float. Note: only events passing the center of the float may be detected by both sonars, and no indication of breaking intensity is given.

that, on average, dissipation values are about 60 times $\varepsilon_{wl} = u_{*w}^3/(\kappa|z|)$, the value predicted for a constant stress layer (Fig. 7). Here u_{w*} is the friction velocity in the water and $\kappa = 0.4$ is the von Kármán constant. However, the mean enhancement ratio, that is, the ratio between observed dissipation rates and the dissipation rate in a flow of the given speed and distance past a solid wall, is not a representative measure of the underlying physics; the observed dissipation values do not have a lognormal distribution. The dissipation enhancement is defined as $r_\varepsilon = \log\{\varepsilon/[u_{w*}^3/(\kappa|z|)]\}$, where the depth z is the streamline of the wave orbital deformation at 1 m from the instantaneous surface, as discussed below. However, here we take a fixed value of $z = -1$ m. For extremely steep waves this might cause the depth to be overpredicted (underpredicted) beneath the crests (troughs) by up to a factor of 2. The observed probability distribution of dissipation enhancement r_ε is a combination of two nearly Gaussian distributions: (i) a broad distribution about the predicted dissipation level $r_\varepsilon = 0$ for a law-of-the-wall boundary layer overlapping (ii) a narrow distribution centered at $r_\varepsilon = 2$. The highly enhanced distribution in point ii contributes to about 25% of the total distribution and is directly linked to breaking waves as discussed below.

All previous near-surface dissipation studies reported average dissipation values, where the averaging period ranged from tens of seconds to several minutes. Aver-

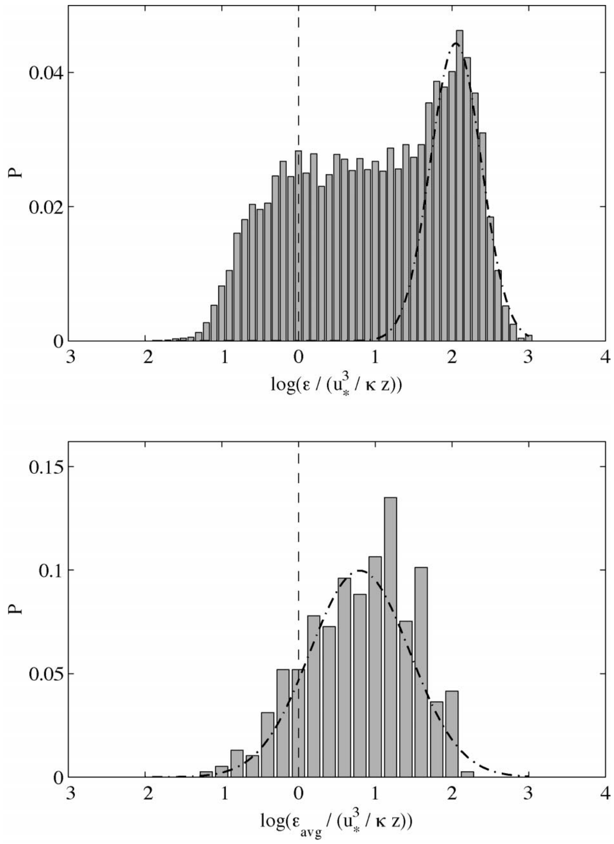

FIG. 7. Distribution of normalized dissipation, based on vertical sonar measurements, for deployment I. The dashed–dotted lines depict lognormal distributions. (top) One-second dissipation average; (bottom) same data using a 60-s time average.

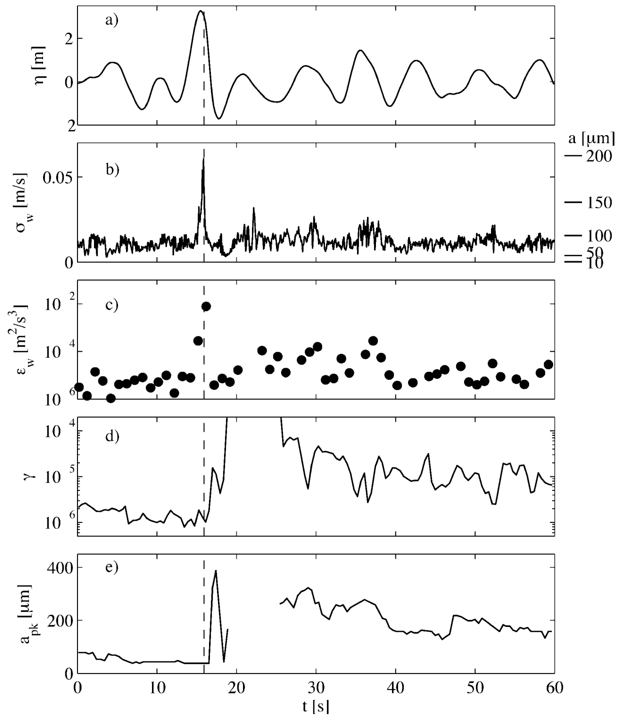

FIG. 8. Float measurements related to the breaking event shown in Fig. 9. Time $t = 0$ corresponds to 0944:00 UTC 10 Oct 2000. The dashed broken line depicts the time when the whitecap reaches the float at $t = 15.9$ s. (a) Surface elevation η obtained with full float motion correlation, (b) standard deviation $\sigma(w)$ of the vertical velocity profile at 0.84–1.6 m beneath the free surface, (c) energy dissipation ε obtained from vertical velocity, (d) air fraction γ at 0.85 m, and (e) peak radius a_{pk} of bubble size distribution at 0.85 m. Bubble radii a corresponding to rise velocities are shown on the right of (b).

aging dissipation data over these time periods greatly modifies their apparent distribution. This can be seen by filtering the dataset used for Fig. 7a, originally obtained at 1-s intervals, with a 60-s filter:

$$\log(\varepsilon_{av}) = \frac{1}{N}\sum_{i=1}^{N}\log(\varepsilon_i), \qquad N = 60. \qquad (7)$$

For this averaged dissipation ε_{av} a very different, monomodal, distribution is found (Fig. 7b). The peak at high dissipation enhancements disappears and only a single 1-min average satisfies $r_\varepsilon > 2$, implying that the observed high dissipation enhancement represents short events. The reduction of occurrences with $r_\varepsilon < 0.2$ suggests that periods consistent with constant-stress layer scaling or less dissipation are also short-lived events in this wind-driven layer. Of course, the mean of the enhancement does not depend on the averaging period. Even the longer period averages do not follow a lognormal distribution.

b. Individual wave analysis

An example of the turbulence and air entrainment associated with an individual breaking wave is shown in Fig. 8. Corresponding video images of the breaking wave are given in Fig. 9. Note that the instrument is moving in and out of the turbulence patch, yielding a bias toward crest samples (Fig. 10). No other breaking waves are observed in the vicinity of this wave or within 60 s prior to or after the event. Thus, the recorded signal can be attributed to an individual breaking wave. The period of this wave, obtained from the horizontal velocity record, is $\tau = 5$ s (Fig. 8a). This is in good agreement with the wave period $\tau = 5.4$ s, corresponding to the propagation speed c_{wc} of the whitecap, estimated from the video recording and assuming linear wave dispersion: $\tau = 2\pi c_{br}/g$. Here g is the gravitational acceleration and $c_{br} = 1.4c_{wc}$ the phase speed of the breaking wave (Lamarre and Melville 1994).

The breaking occurs near the crest of the largest wave of the wave group (Fig. 8a). Note that, due to the float motion, different wave phases are sampled with different spatial resolution, making the wave time series appear asymmetric as discussed subsequently. The spatial transformation for this wave is given in (Fig. 11c). Significant velocity fluctuations occur during passage of the whitecap at $t = 15.9$ s. The standard deviation of the vertical velocity within each individual

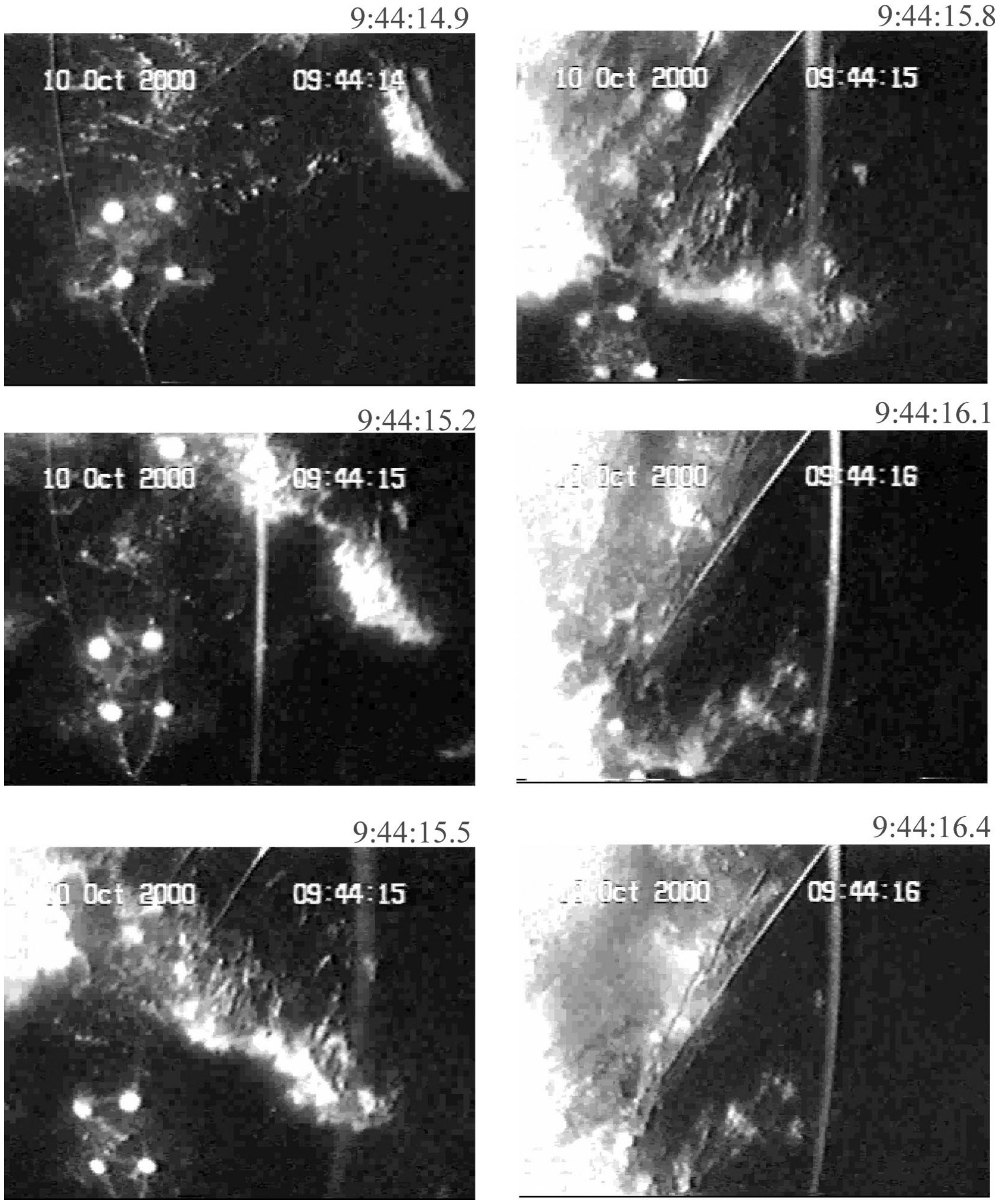

FIG. 9. Video images corresponding to 1.5 s of the breaking event shown in Fig. 8. Time stamps are given above each image. The float (four circles) is in the lower-left corner of the image.

profile $\sigma(w)$ increases rapidly from about 1×10^{-2} to 6×10^{-2} m s^{-1} (Fig. 8b). The duration of the intense fluctuations is 1.2 s or approximately one-quarter of the wave period. Figures 11a,b show a more detailed presentation of the vertical velocity field. The top of the measurement profile, which is 1 m below the instantaneous surface, cuts through near-surface streamlines due to the wave orbital deformation. In Fig. 11b data have been mapped onto a coordinate system fixed at the instantaneous surface, but depth coordinates are stretched so as to represent the instantaneous streamlines. Velocity fluctuations at the onset of breaking occur along the entire velocity profile. The velocity field is divided into the depth-averaged component $\langle w \rangle$ and the fluctuating part w'. The coherent signal results mainly from rapid oscillations of the float and a weak signal of the differential orbital velocity (appendix). The incoherent signal is somewhat stronger than the coherent component. The strongest signal occurs at the onset of breaking at the crest of the wave. Fluctuations diminish rapidly when the float drifts out of the most active turbulent patch. The subsequent wave crest ad-

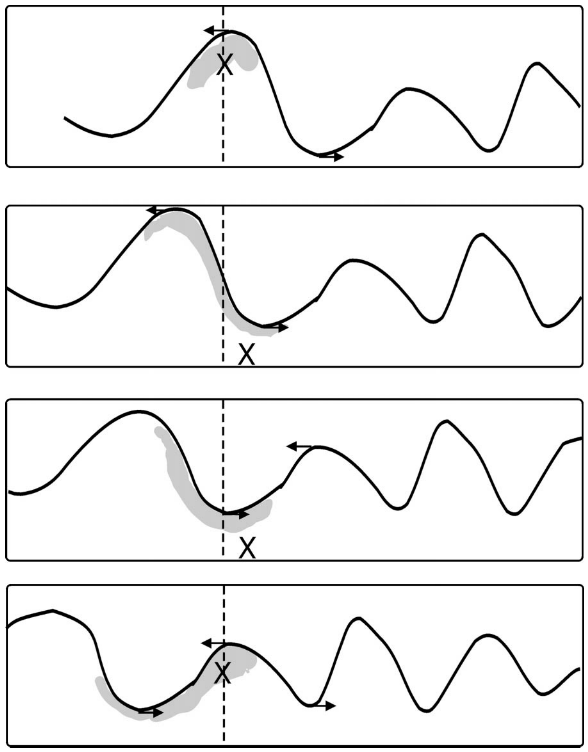

FIG. 10. Sketch showing the simplified distortion of a turbulence patch (gray area) by subsequent waves. The location of the turbulence measurements is marked by $\times$. The arrows indicate the wave orbital motion.

vects the float back into the turbulent patch, resulting in increased w' (i.e., $t = 20$–21 s).

Prior to the breaking event, the inertial subrange of the velocity spectra spans 20–160 rad m^{-1} (Fig. 12). At the onset of breaking, energy increases across the spectrum but particularly at high wavenumbers, $k > 100$ rad m^{-1}. Energy in the high wavenumber range dissipates rapidly. Approximately 1.5 s past the onset of breaking, the peak of the energy spectrum has shifted to $k \approx 20$ rad m^{-1} from an initial peak at $k \approx 150$ rad m^{-1} at the beginning of the breaking event. Roughly within the following one second, the spectrum reassumes a spectral form consistent with an inertial subrange.

The background dissipation prior to the breaking event is $O(5 \times 10^{-6}$ m^2 s$^{-3})$ (Fig. 8c). The maximum resolved dissipation is 8×10^{-3} m^2 s^{-3} and occurs when the whitecap passes above the sonar. It is interesting to note that 0.7 s prior to the whitecap arrival the dissipation has already increased to 100 times the background level. Within the first second following the breaking event, no inertial subrange was present in either the full profile or the near or far field, and no dissipation can be estimated. Therefore, the observed dissipation enhancement $r_\varepsilon = O(5 \times 10^2)$ is a lower bound for the turbulence associated with this individual wave. Enhanced turbulence levels persist for at least 10 wave periods. The average dissipation rate in the first 10 wave periods following the breaking event is 5×10^{-5} m^2 s^{-3}. However, the dissipation fluctuates periodically by two orders of magnitude. High dissipation rates $O(10^{-4}$ m^2 s$^{-3})$ reoccur at intervals similar to the wave period. A probable explanation of the periodicity of turbulence intensity might be the stretching of the turbulence patch due to wave orbital motion, combined with the instrument movement in and out of the turbulence patch (Fig. 10).

Air fraction, which is an integral measurement within the upper 0.2 m of the velocity profile, shows a clear signature of the wave breaking (Fig. 8d). Prior to the event, the air fraction was of the order of 5×10^{-6}. Approximately 1 s after the whitecap reaches the float at the surface, the air fraction at 0.85-m depth increases rapidly and reaches the saturation level of the resonator (10^{-4}) about 3 s after the crest has passed the event. Air fraction stays at this high level for close to two wave periods and decays slowly afterward. Ten wave periods after the event, the average air fraction is more than twice the value prior to the breaking event.

The peak bubble radius prior to the breaking event is $a_{pk} < 100$ μm. Air entrainment associated with the whitecap passage transports larger bubbles down to the depth of the upper resonator, resulting in a peak bubble radius >300 μm. The maximum velocity fluctuations of ~ 0.06 m s^{-1} are sufficient to counteract the rise velocity of bubbles with 200-μm radius (Fig. 8b). The more persistent turbulent velocity field generated by the breaking event may keep bubbles with circa 120-μm radius in suspension. This is consistent with the observed bubble size distribution. Approximately 10 s after the air injection the larger bubbles have disappeared at the sensor depth and the peak bubble radius slowly decreases (Fig. 8e). The majority of the remaining suspended bubbles have radii smaller than 120 μm.

Figure 13 shows more examples of turbulence data related to breaking events. In all cases the whitecap passage is associated with increased turbulence. However, if the breaking event is not discrete but occurs as a succession of smaller breaking events over one or two wave periods, several peaks in the turbulence signals are common (e.g., Figs. 13d,e,h,j).

4. Discussion

a. Characteristic turbulence signal of breaking events

The individual breaking wave discussed above in detail shows a distinct turbulence and air-fraction signature common to most strong breaking events. For a further systematic analysis of the wave-induced signal, wave-breaking data for 0930–1330 UTC 10 October are conditionally sampled and averaged. During this 4-h period of nearly steady wind, 31 single breaking events with significant air fraction [$\gamma(0.85$ m$) > 3 \times 10^{-5}$, corresponding to the 95th percentile of the air-fraction record] were detected. The development stage of whitecaps

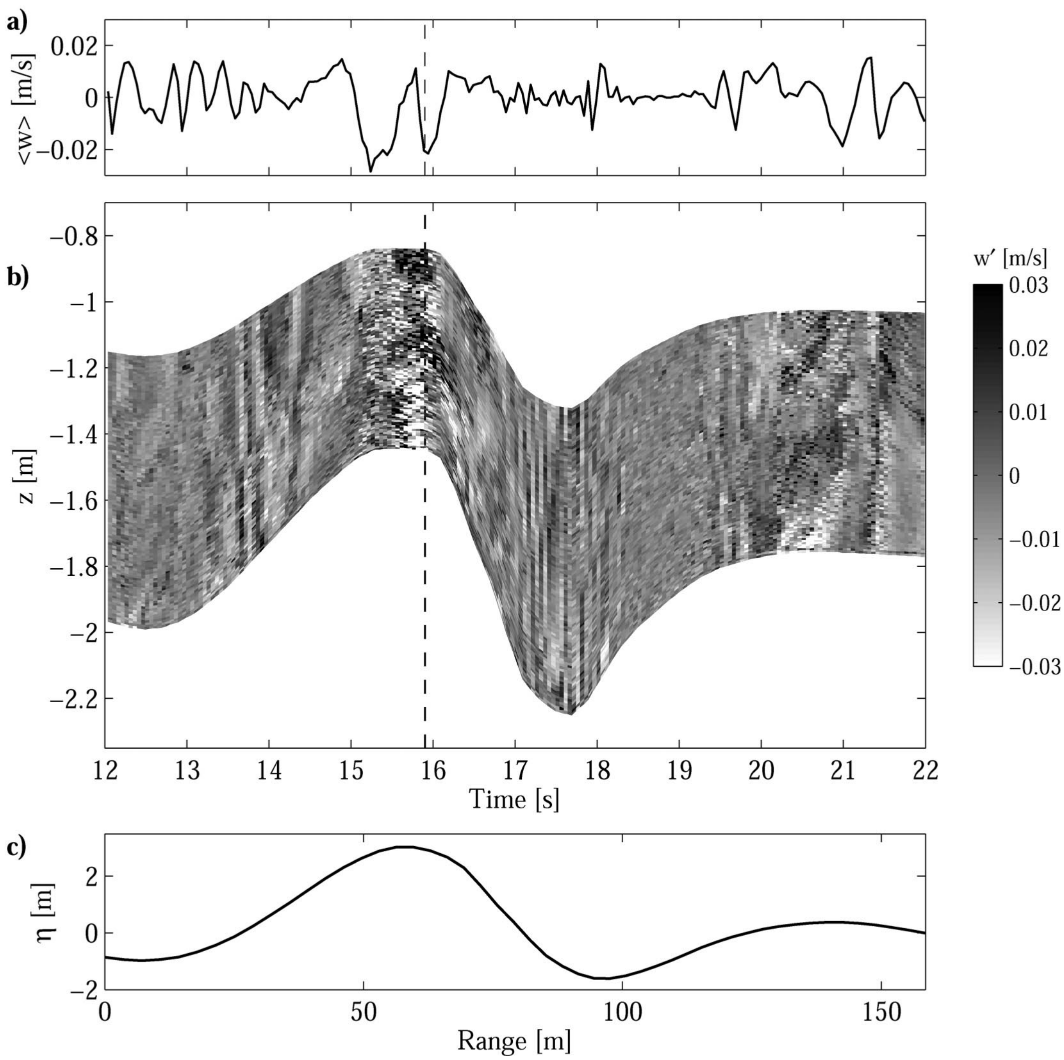

FIG. 11. Velocity field associated with the breaking event shown in Fig. 8 (dashed line). (a) Range-average vertical velocity $\langle w \rangle$. (b) Fluctuating vertical $w' = w - \langle w \rangle$. Depth z represents the encountered near-surface streamlines. The top of the measurement profile is located 1 m below the instantaneous surface and cuts through near-surface streamlines because of the wave orbital distortion. (c) Surface elevation η in wavenumber space, where the transformation is based on the local wave phase speed corrected by the observed float displacement speed.

reaching the float covers a wide range, and the onset of increased turbulence occurs within ± 1 s of the whitecap passage (Fig. 13). Assuming that a whitecap is generated near the crest, we center the time series of individual breaking waves at the occurrence t_b of the crests associated with the breaking events, not the whitecap passage, and normalize it by the local wave period τ_w: $\tilde{t} = (t - t_b)/\tau_w$. The crest association is based on the ''riding wave removal'' (RWR) approach developed by Banner et al. (2002).

The RWR method progressively detects and removes riding waves through iterative processing starting with the highest frequency resolved. Occurrence and characteristic dimensions of riding waves are retained in a file and the waves are then removed from the elevation series by replacing it with a cubic polynomial spliced to the underlying longer wave form. Subsequently, the association between breaking events and recorded waves is based on minimizing the relative lag between the time of the breaking event and the time of the nearest local crest, while also satisfying a local steepness threshold $\tilde{a}k > 0.075$, where $\tilde{a}$ and k are the local apparent wave amplitude and wavenumber. The occurrence time t_b and wave period τ_{RWR} of the breakers are then recorded to file. Generally, there is good agreement between the wave period estimates from the whitecap propagation and the RWR-modified surface elevation.

Figure 14 shows the conditionally sampled average evolution of dissipation and bubble characteristics associated with wave breaking. The time series includes two wave periods prior to the breaking event and the five subsequent waves. Before averaging, each individ-

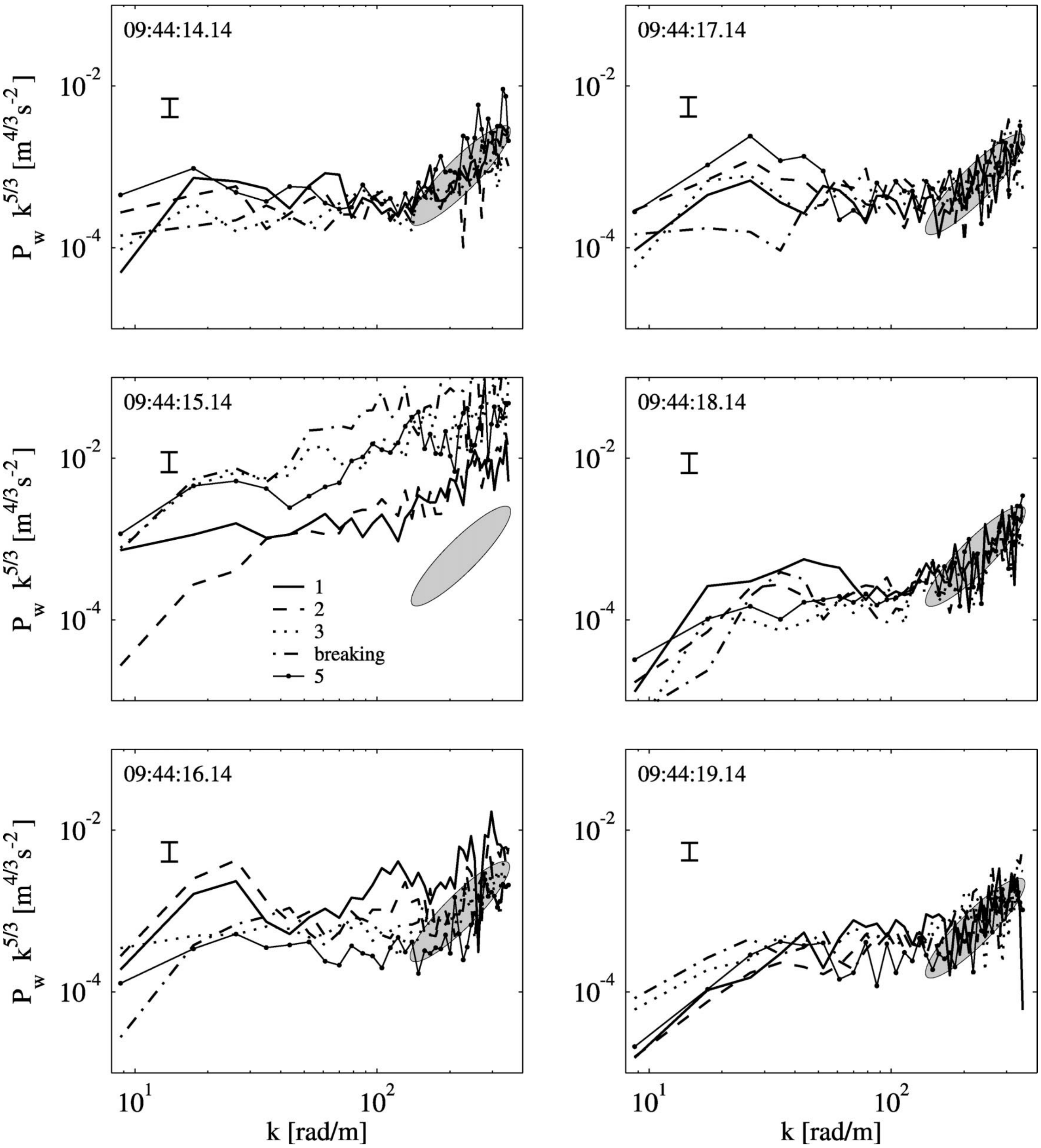

FIG. 12. Scaled velocity spectra associated with the breaking event shown in Fig. 8. Each spectrum is an average of four individual raw spectra, yielding 5-Hz sampling. Start time of first spectrum (solid) is given in top-left corner. Subsequent spectra are presented as dashed, dotted, dash–dot, and line–dot lines, respectively. The gray area depicts the approximate noise level; the error bar represents one standard deviation.

ual time series is normalized by its extreme value within these seven wave periods. In case of the surface elevation, normalization is done with respect to the maximum surface elevation. Dissipation, air fraction, and peak bubble radius cover a wider dynamic range, and it is possible that the maximum value, associated with the breaking event, is not resolved properly. Therefore, these quantities are normalized by their minimum value, which represents background conditions not directly affected by the breaking event and is less sensitive to sensor saturation. It is important to note that the RWR method is used only to determine the properties t_b and τ_{RWR} of the breaking wave. The conditional sampling is based on the original records and therefore does not involve any filtering of the turbulence signal.

The breaking crest is generally the highest crest within the wave group, roughly 50% higher than the previous or subsequent crests (Fig. 14a). Associated with the breaking crests are the largest dissipation levels. Turbulence signals associated with multiple breaking events

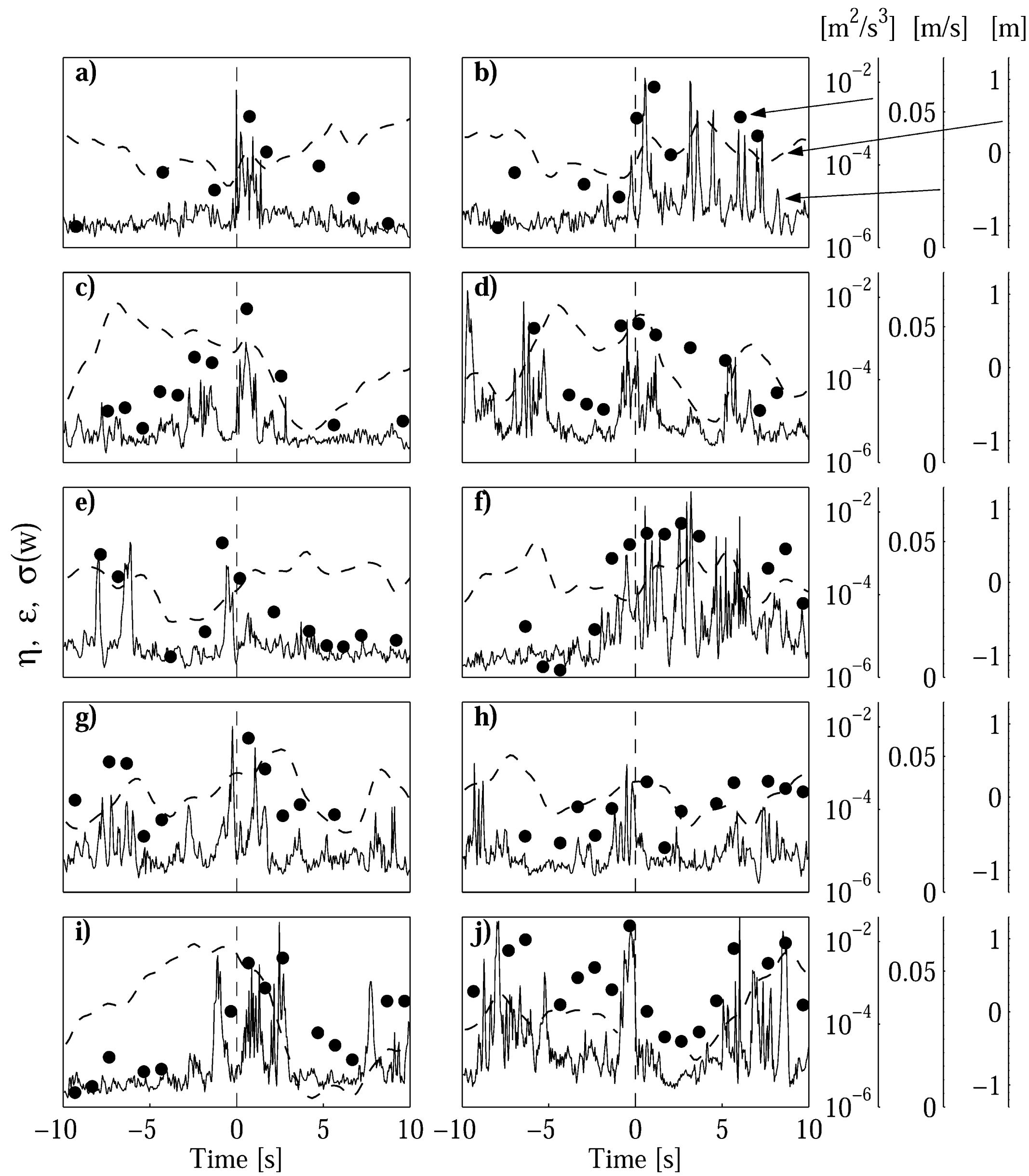

FIG. 13. Float measurements related to 10 breaking events, including single and multiple breakers (1000–1030 UTC 10 Oct 2000). Time series of surface elevation η (dashed line, uncorrected for float movement), standard deviation of vertical velocity profile $\sigma(w)$ (solid line), and dissipation ε (dots) are centered at the time when the main whitecap reaches the float (dashed vertical line); i.e., $t = 0$ s. Axes on the right show scaling for ε, $\sigma(w)$, and η, respectively, which are the same for all panels.

are incoherent and the conditional sampling technique tends to average them out. Dissipation associated with the main breaker increases rapidly on the forward face of the wave crest. No reliable dissipation estimates could be obtained in the direct vicinity of the breaking crest. It is possible that the resolved dissipation does not include the maximum value and the observed 3000-fold increase represents a lower bound for the dissipation beneath breaking waves. Nevertheless, the data clearly demonstrate high turbulence levels generated by the breaking wave. Comparison with the bubble observations shows that the increase in turbulence occurs up to a quarter wave period *prior to* the bubble cloud reaching the sensor depth (Figs. 14c,d). This delay between TKE dissipation and bubble injection is very prominent, even in this averaged signal, and is a general feature of the observed turbulence induced by breaking waves. Thus, wave-enhanced turbulence is caused not only by air entrainment and the associated conversion of potential energy to turbulent kinetic energy but by dynamical pro-

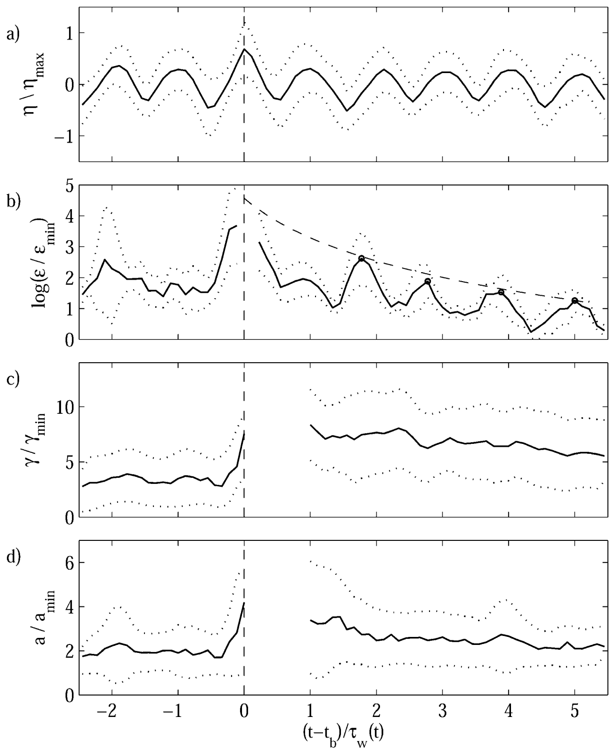

FIG. 14. Average signal associated with wave breaking (0930–1330 UTC 10 Oct 2000): (a) Normalized surface elevation, (b) normalized dissipation and inferred turbulence decay for decay rate $n = -4.3$ (dashed line), (c) normalized air fraction γ, and (d) normalized peak radius of bubble size distribution. The time axis is normalized by the local wave period and centered at the passage of the breaking crest (not necessarily the leading edge of the whitecap). Dotted lines represent one standard deviation.

cesses related to the steep wave itself. Indeed, enhanced turbulence might be a prerequisite for the breakup of the surface and bubble generation. A probable source of turbulent kinetic energy is discussed below.

Following the turbulence generation by the breaking wave, the observed dissipation fluctuates with local maxima coinciding with the forward face of the subsequent waves. These fluctuations are not primarily related to the evolution of the turbulent patch but rather to the motion of the float with respect to the turbulence combined with a possible wave-induced stretching of the turbulence patch. The wave orbital motion prior to passage of the crest advects the float into the center of the turbulence patch, whereas on the rear face of the wave the float is pushed farther to the edge of the patch. It is unlikely that the observed dissipation fluctuations are linked to the persistent near-surface vortex generated by the breaking event (Melville et al., 2002) since the vortex setup takes several wave periods.

The evolution of the maximum dissipation within waves following the breaking event (circles in Fig. 14b) indicates the decay of the wave-induced turbulence. Again, the dissipation in the direct vicinity of the breaking crest is not resolved, and we can only give bounds for the decay rate $\varepsilon \propto t^n$, based on a least squares fit of the marked maxima in Fig. 14b. Assuming that the resolved dissipation includes the maximum value, we find the lower bound $n = -2.9$. If, however, as is much more likely, the largest dissipation is not measured and occurs closer to the crest, the highest observed value (at $\tilde{t} = -0.25$) has to be excluded from the least squares fit. This case, where the decay rate is determined from observations two to five wave periods after passage of the crest, defines the upper bound of the decay rate $n = -4.3$. Extrapolating this decay backward yields a maximum enhancement rate at the breaking crest $\log(\varepsilon_{\max}/\varepsilon_{\min}) \approx 4.6$, which serves as an upper bound for the average dissipation beneath breaking waves. The upper bound of the decay rate $n = -4.3$ is in good agreement with the theoretical dissipation decay rate for isotropic turbulence, $n = -17/4$ (Hinze 1975). This supports our assumption of isotropic wave-induced turbulence in the near-surface region. We should not expect isotropic turbulence to occur very close to the boundary, and we note here that a much faster decay rate ($n = -7.6$) was inferred in the upper 0.2 m of the water column where dense bubble clouds lead to stratification (Gemmrich 2000).

Air fraction beneath individual breaking waves fluctuates rapidly and over a wide range that exceeds the resonator saturation. Nevertheless, the average air fraction signal (Fig. 14c) highlights the rapid increase in air fraction beneath the breaking crest. The brief large air fractions beneath the rear face of the breaking wave (Gemmrich and Farmer 1999b; Deane and Stokes 2002) cannot be resolved with the present instrumentation. However, the presence of air bubbles can be tracked for at least five wave periods following the breaking event. These increased air fractions are associated with a rapid shift in the bubble size distribution toward larger radii (Fig. 14d) following passage of the breaking event.

The breakup of air bubbles beneath breaking waves is the direct result of turbulent pressure fluctuations and thus there exists a relation between bubble sizes and dissipation. The Hinze scale a_H describes the maximum bubble radius sustained by surface tension, with larger bubbles being disrupted by the turbulent pressure forces (see Garrett et al. 2000):

$$a_h = c(\gamma_w/\rho)^{3/5}\varepsilon^{-2/5}, \tag{8}$$

where γ_w is the surface tension, ρ the water density, and the constant c ranges between 0.36 and 0.5. Our estimate of the maximum dissipation $\log(\varepsilon_{\max}/\varepsilon_{\min}) = 4.6$ and $\varepsilon_{\min} = 5 \times 10^{-6}$ m^2 s^{-3} (Fig. 6) yields $a_H \approx 2 \times 10^{-3}$ m. This is in good agreement with the Hinze scale found by Deane and Stokes (2002). Garrett et al. (2000) argued that the widely seen small bubbles with $a = O(100\ \mu\text{m})$ are generated by intermittent high dissipation rates $O(10\text{–}100$ m^2 s$^{-3})$ at the point of air entrainment.

b. Wave–turbulence interaction

Laboratory and field studies have shown that surface waves may not be considered entirely irrotational. [For a short review of these experiments see, e.g., Anis and Moum (1995)]. In a rotational wave field, interactions between the mean, wave, and turbulence components of the flow provide additional TKE sources not present in a wall layer flow. The possible wave–turbulence interactions are best identified in the respective kinetic energy equations. For that purpose the velocity and pressure records are separated into a mean, wave-related, and turbulence contribution: $v_i = V_i + \tilde{v}_i + v_i'$, $i = 1$–3, $p = P + \tilde{p} + p'$, where the wave–turbulence separation is achieved by the phase-averaging method (e.g., Thais and Magnaudet 1996). Assuming a mean flow in the x direction, the kinetic energy of the mean flow (MKE), the wave orbital flow (WKE), and turbulence (TKE) are

$$K = \frac{1}{2}UU, \qquad \tilde{k} = \frac{1}{2}\tilde{v}_i\tilde{v}_i, \quad \text{and} \quad k_t = \frac{1}{2}v_i'v_i', \tag{9}$$

respectively. The resulting equations are for MKE:

$$\frac{dK}{dt} = \underbrace{\overline{\tilde{u}\tilde{w}}\frac{\partial U}{\partial z}}_{\text{(a)}} + \underbrace{\overline{u'w'}\frac{\partial U}{\partial z}}_{\text{(b)}} - \underbrace{U\frac{\partial}{\partial x}\left(\frac{P}{\rho}\right)}_{\text{(c)}} - \underbrace{\frac{\partial}{\partial z}(\overline{u'w'U})}_{\text{(d)}}, \tag{10}$$

for WKE:

$$\frac{\overline{d\tilde{k}}}{dt} = -\underbrace{\overline{\tilde{u}\tilde{w}}\frac{\partial U}{\partial z}}_{\text{(a)}} + \underbrace{\overline{\widetilde{v_i'v_j'}\frac{\partial \tilde{v}_i}{\partial x_j}}}_{\text{(b)}} - \underbrace{\frac{\partial}{\partial z}\left(\overline{\frac{\tilde{p}}{\rho}\tilde{w}}\right)}_{\text{(c)}} - \underbrace{\frac{\partial}{\partial z}(\overline{\widetilde{v_i'v_j'}\tilde{v}_i})}_{\text{(d)}} - \underbrace{\frac{\partial}{\partial z}(\overline{\tilde{k}\tilde{w}})}_{\text{(e)}}, \tag{11}$$

and for TKE:

$$\frac{\overline{dk_t}}{dt} = -\underbrace{\overline{u'w'}\frac{\partial U}{\partial z}}_{\text{(a)}} - \underbrace{\overline{\widetilde{v_i'v_j'}\frac{\partial \tilde{v}_i}{\partial x_j}}}_{\text{(b)}} - \underbrace{\frac{\partial}{\partial z}\left(\overline{\frac{p'}{\rho}w'}\right)}_{\text{(c)}} - \underbrace{\frac{\partial}{\partial z}(\overline{k_t w'})}_{\text{(d)}} - \underbrace{\frac{\partial}{\partial z}(\overline{\tilde{k}_t\tilde{w}})}_{\text{(e)}} - \underbrace{\varepsilon}_{\text{(f)}}. \tag{12}$$

Averaging periods much longer or comparable to the wave period are indicated by overbars and tildes, respectively.

Beneath a breaking crest, the approximate balance between dissipation [(12), term f] and turbulent diffusion of TKE [(12), term d] results in the observed large dissipation values. However, prior to the onset of breaking the diffusion term has to be much smaller and the increased dissipation may be balanced by TKE production based on wave–turbulence interaction. From (10)–(12) it can be seen that there exist two possible pathways to convert WKE into TKE, one indirect and one direct way.

In the indirect pathway, wave energy is transferred to the mean flow and then in turn into turbulence as follows. The wave-induced shear stress in a mean current shear [(11), term a] transfers energy from the waves to the mean current [(10)]. The MKE may then be redistributed into TKE through the classical production term [(10), term b]. Assuming a steady-state balance between dissipation and shear production yields (Anis and Moum 1995)

$$\varepsilon \approx \frac{1}{2}a^2gke^{2k|z|}\sin\phi\frac{\partial U}{\partial z}, \tag{13}$$

where ϕ is the deviation from quadrature of u and w, and a and k are wave amplitude and wavenumber, respectively. Taking representative values $a = 1.5$ m, $k = 0.01$ m^{-1}, and the observed mean current shear $\partial U/\partial z \approx 0.01$ s^{-1} suggests that a small phase shift $\phi = 6°$ is sufficient to generate enhanced dissipation levels $\varepsilon = O(10^{-3}$ m^2 s$^{-3})$, observed at the onset of breaking. Phase differences of this magnitude are fully consistent with those previously reported in the literature (see Anis and Moum 1995). A rough estimate of the u–w phase shift can be obtained from the cross-spectral analysis between the surface elevation time series derived from the horizontal velocities and the observed vertical velocity field, as follows. The float follows the surface motion and therefore the observed vertical velocity is reduced to a residual wave orbital motion (appendix):

$$w_{\text{obs}}(z) = w(z) - w(z_F). \tag{14}$$

For a better comparison with the observed vertical velocity, the surface elevation signal will be reduced, based on linear relations, to a signal corresponding to $w_{\text{obs}}(z)$. The instantaneous wave frequency ω is obtained from the surface elevation time series in analogy to (4) as $\omega(t) = d\theta/dt$. This method is only valid for narrowband signals, and therefore the intrinsic mode decomposition (Huang et al. 1998) is applied before the weighted-average frequency of all modes is calculated. Based on this frequency, using the linear dispersion relation $k = \omega^2/g$ and the surface elevation record, the vertical component of the wave orbital motion of irrotational deep-water waves is modeled as

$$w_{\text{ir}}(z) = H(\eta)\omega(e^{-k|z|} - 1). \tag{15}$$

For irrotational waves, there is no phase difference between $w_{\text{obs}}(z)$ and $w_{\text{ir}}(z)$. We calculated the coherence and phase between $w_{\text{obs}}(z)$ and $w_{\text{ir}}(z)$ for all depth bins for a 10-min record during deployment III. Despite the approximations involved in this method, about 10%–25% of the estimates pass the 95% confidence level and from these estimates an average phase relation is then calculated. In the frequency range of the wind waves, we find a phase shift $\phi \approx 17°$, which is sufficient for significant TKE production by wave–turbulence interaction. However, wave tank experiments have also revealed positive wave stresses leading to energy transfer from MKE to WKE, and therefore this indirect wave–turbulence interaction cannot be considered general (Thais and Magnaudet 1996).

The direct mechanism for wave–turbulence interaction occurs through term b in (11) and (12), representing the Reynolds stresses working against the shear of the rotational component of the wave orbital motion (Thais and Magnaudet 1996). This mechanism requires that the turbulent time scale T_t is much shorter than the wave period τ, $T_t \ll \tau$. On dimensional grounds this leads to following conditions for the turbulent velocity scale $u_t \ll (T\varepsilon)^{1/2}$ and the turbulent length scale $l_t \ll \tau u_t$ (Anis and Moum 1995). Here we get $u_t \ll 0.1$ m s^{-1} and $l_t \ll 1$ m, and conditions are favorable for this mechanism to be relevant. Thais and Magnaudet (1996) conclude that microbreaking and capillary ripples are the most obvious candidates for the required vorticity generation. These small-scale features may then also trigger larger-scale breaking. Hence, the direct wave–turbulence interaction would be strongest on the forward face of a wave crest and therefore would occur prior to the white-cap passage, consistent with video recordings of the analyzed breaking event. Indeed, recent laboratory studies of microbreakers using infrared imager and particle image velocimetry revealed strong near-surface vorticity in the crest region of microbreakers (Siddiqui et al. 2001).

Here we have shown possible mechanisms for the generation of near-surface turbulence. Recently, Teixeira and Belcher (2002) studied the interaction of weak near-surface turbulence with a monochromatic irrotational wave. They report that the distortion of the turbulence by the Stokes drift leads to the generation of Langmuir turbulence and also produces additional shear stresses. These stresses work against the straining of the wave orbital motion and thus, over many wave periods, further convert WKE into TKE.

c. Depth dependence

In the classical wall-layer flow dissipation decreases with distance from the boundary as $\varepsilon(z) \propto |z|^{-1}$. Field observations suggest that in a wind-driven sea the surface layer may be divided into three regimes (Terray et al. 1996). Wave breaking directly injects turbulent kinetic energy into the top layer to depth z_b. In this injection layer dissipation is highest and depth independent. Below that depth the wave-induced turbulence diffuses downward and dissipates. In this region of wave-induced turbulence the turbulence decay rate with respect to depth is steeper than for wall-layer dependence. At a depth z_t, sufficiently far from the air–sea interface, the contribution of wave-induced turbulence

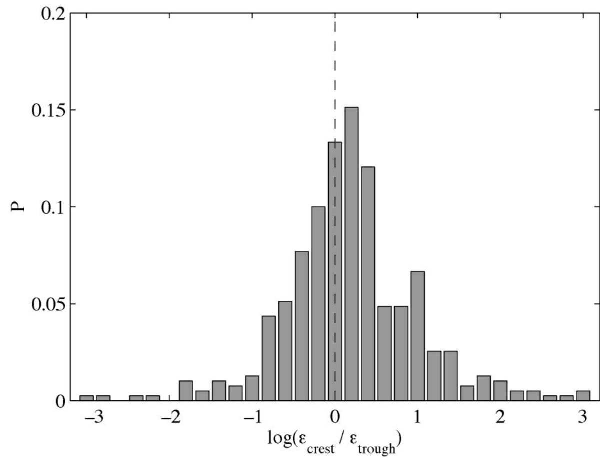

FIG. 15. Distribution of ratios of mean dissipation beneath crests and troughs of individual waves, including breaking and nonbreaking waves (deployment I).

becomes small compared to local shear production and turbulence properties are well described by the constant-stress-layer scaling. The problem is complicated by the strong temporal and spatial variability of the turbulence as exemplified by our observations. There is no conclusive observational evidence for the vertical extension of the different regimes (z_b, z_t) nor the exact depth dependence of the wave-induced turbulence. For the latter, the scaling $\varepsilon \propto |z|^n$, $n = -2$ to -4 (Terray et al. 1996; Drennan et al. 1991), has been suggested, as well as exponential decay $\varepsilon \propto e^{-|z|}$ (Anis and Moum 1995). Also, there are no observations verifying the existence of a constant dissipation layer at the surface. In their pioneering study, Stewart and Grant (1962) argue that more than one-half of the energy is dissipated above the mean waterline. Therefore, dissipation levels at a fixed distance beneath a crest and beneath a trough should differ, contradicting the assumption of a constant dissipation layer. To a certain extent, our surface-following measurements allow us to evaluate the vertical structure of the near-surface dissipation field, particularly with respect to the wave phase.

We calculate the average dissipation beneath a wave crest, defined as the period between zero-up crossing and zero-down crossing of the RWR-filtered surface elevation and the average dissipation of the subsequent trough. To avoid potential biases due to the unknown intermittency of near-field and far-field dissipation estimates, the following analysis is based on dissipation estimates obtained from entire velocity profiles only. The distribution of the ratio $\varepsilon_{crest}/\varepsilon_{trough}$ for each individual wave (including breaking and nonbreaking) is given in Fig. 15. Cases with crest dissipation values larger and smaller than the dissipation beneath the trough region are found. However, there is a clear bias toward crest dissipation being larger than the trough dissipation. The average ratio is $\varepsilon_{crest}/\varepsilon_{trough} \approx 1.6$. Our observations are made 1 m below the free surface. Only

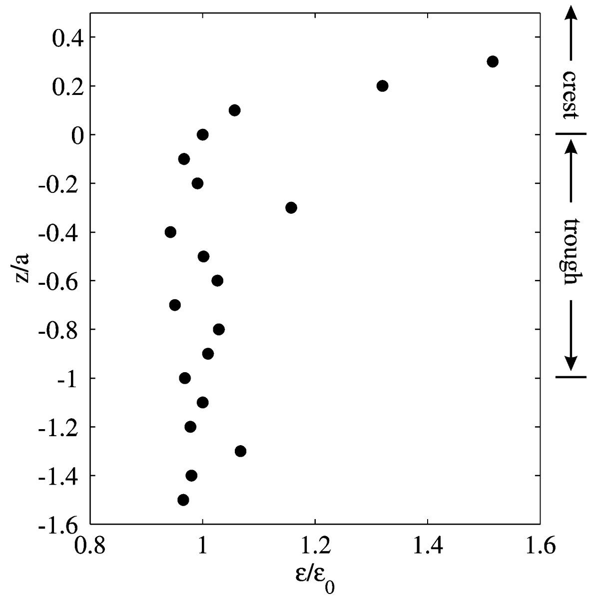

FIG. 16. Conditionally sampled averaged dissipation profile beneath waves (deployment I). Depth z is relative to still water level and normalized by wave amplitude a; dissipation ε is normalized by the individual value ε_0 at $z/a = 0$.

for waves with amplitude $a \gg 1$ m do the crest dissipation measurements represent conditions above the mean waterline. We conclude that our observations are consistent with Stewart and Grant's (1962) reasoning.

Depending on the individual wave amplitude a_i and the phase of the wave, our observations profile the water column over the range $z_s - a_i \leq z \leq z_s + a_i$, where depth z is referenced to the mean surface elevation averaged over the wave period (positive upward) and $z_s = -1$ m is the sensor depth. Normalizing the depth by the wave amplitude and sorting the results in depth bins gives information on the dissipation profile beneath waves. Each profile is then normalized by its value $\varepsilon_0 = \varepsilon(z = 0)$ and all profiles are bin averaged (Fig. 16). Below the mean waterline dissipation stays nearly constant. However, in the crest region dissipation increases rapidly as $\varepsilon \propto z^{2.3}$. Extrapolating the dissipation to the crest ($z/a = 1$), we find that the total dissipation (depth integrated per unit area) in the region above the mean waterline is about 2.5 times the total dissipation between the trough line and the mean waterline. Our observations reach to a maximum depth 1 m below the actual wave troughs; therefore, we do not have reliable depth dependence below approximately $z/a < -1.5$. It should be noted that the dissipation structure suggested by Terray et al. (1996) is based on a fixed coordinate system and mainly acquired from tower observations, which excluded the region above the trough line. Since the region above the trough line is the most active part of the water column, it is more appropriate to use a wave-following coordinate system for the analysis of near-surface turbulence measurements.

Models of near-surface turbulence rely on a flat surface, commonly positioned at the mean water level. Burchard (2001) stated that the virtual model origin $z_{\rm org} = z(0)$ should be ''located at the base of the unresolved surface layer'' at $z_{\rm org} = -z_0$, where z_0 is the surface mixing length. However, the conversion from a wavy surface to a flat surface inherent in the model assumes a linear dissipation profile above the trough line. Based on our finding that the dissipation ratio in the trough to crest region is 2:5, we argue that the model origin should correspond to the location of the mean dissipation, which yields $z_{\rm org} = 0.24H_s$, or approximately halfway between the mean waterline and the significant wave crests.

Figure 17a shows a comparison of two recent models with our observations. The models predict a mean dissipation profile that is a function of the friction velocity only. However, Greenan et al. (2001) found that the vertical profile of the mean dissipation is sensitive to the directional distribution of the wave energy. Only for a clear separation between swell and windwaves was the modeled dissipation profile consistent with their observations, which started approximately at 2-m depth and included measurements beyond the shallow mixed layer down to about 18 m. To minimize the effects of processes not included in the model, we limit the model–observation comparison to a case of limited swell effects and with u^* approximately constant. Deployment II took place after several days of nearly steady wind, generating a unimodal wave field propagating from 320° with peak frequency $f_p = 0.11$ Hz, without lower frequency swell. The friction velocity during the deployment stayed nearly constant, allowing a comparison of the mean observed dissipation and the model output. Results are presented in nondimensional form $|z|/H_s$, $\varepsilon H_s/F$, where $F = \overline{c}u_{w*}^2$ is the input of turbulent kinetic energy at the model surface and $\overline{c}$ is the effective phase speed of waves acquiring energy from the wind (Gemmrich et al. 1994). The commonly applied Craig–Banner (1994) model in its modified version (Terray et al. 1999) and the recent generic length-scale model (Umlauf and Burchard 2003) are in reasonable agreement and consistent with the observed mean dissipation rate. The parameters for both models are the input of turbulent kinetic energy $F = \overline{c}u_{w*}^2$, $\overline{c} = 1$ m s^{-1}, and the surface mixing length $z_0 = 0.2$ m (Gemmrich and Farmer 1999a). Placing the model origin at the mean waterline results in modeled dissipation rates that, at the sensor depth, are 1/30–1/40 of the observed value. This supports our assumption of $z_{\rm org} \approx H_s/4$. A critical parameter of these models is the surface mixing length z_0. Here we have set $z_0 = 0.2$ m, based on the observed scale of temperature fine structures (Gemmrich and Farmer 1999a), which is significantly smaller than $z_0 = 0.6H_s$ found by Soloviev and Lukas (2003) and $z_0 \approx H_s$ suggested by Terray et al. (1996). However for $z_{\rm org} = 0$ the models do not reproduce the observed dissipation for any choice of z_0 (Fig. 17b) and neither for $z_{\rm org} = -z_0$.

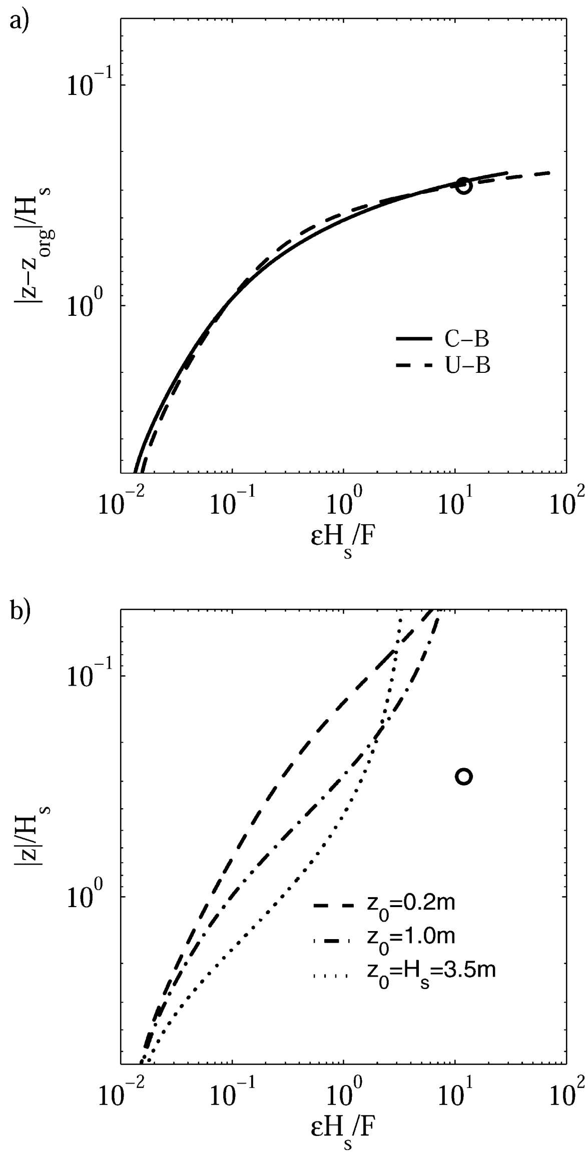

FIG. 17. Average observed dissipation during deployment II (circle) and corresponding modeled dissipation profile. The models assume a virtual, flat surface. (a) Model surface located halfway between the significant wave crests and the mean waterline. Craig–Banner parameterization (solid line) and Umlauf–Burchard generic length-scale model (dashed line), both with $z_0 = 0.2$ m. (b) Model surface located at the mean waterline. Umlauf–Burchard parameterization for different values of z_0 as shown in legend.

In light of the strong depth dependence of dissipation it becomes clear that the assumption of a flat surface at the mean waterline cannot represent wave-induced turbulence. This holds in the near-surface area, at least to a depth much larger than the significant wave height.

Based on the modeled dissipation profile (Fig. 17) we estimate the total dissipation in the surface layer, $D = \int_0^{z_m} \varepsilon(z)\, dz$, with mixed layer depth z_m. Depending on the model used we find $D = 6.5 \times 10^{-4}$ m^3 s^{-3} (Craig–Banner) and $D = 8.8 \times 10^{-4}$ m^3 s^{-3} (Umlauf–Burchard). Very recently, Melville and Matusov (2002) estimated the energy dissipation in breaking waves from the speed c and distribution of whitecaps, $D = \int c^5\Lambda(c)\, dc$, where $\Lambda(c)dc$ is the average length of breaking crests per unit area. Analyzing aerial imaging of breaking waves they found that the measurements of $\Lambda(c)$ collapse onto a single exponential curve if normalized by the cube of the wind speed. Using this result we find that the average total dissipation during deployment II is $D = 9 \times 10^{-4}$ m^3 s^{-3}. This is in good agreement with the model results and supports the assumption that near-surface energy dissipation is strongly linked to wave breaking.

5. Conclusions

Dissipation measurements from a surface-following float provided new insight on the turbulence structure beneath breaking and nonbreaking waves, including the region above the trough line. Consistent with previous studies we find enhanced near-surface turbulence. However, due to the short averaging period of 1 s we were able to separate the turbulence enhancement due to active wave breaking from the background dissipation resulting from decaying wave-induced turbulence and shear stresses. The short-lived high-dissipation rates are, on average, several hundred times those predicted by constant-stress-layer scaling. Detailed measurements beneath individual breaking events provided a definite link between wave breaking, air entrainment, and enhanced dissipation. The decay of wave-induced turbulence $\varepsilon \propto t^n$ has been observed with bounds for the decay rate of $-4.3 < n < -2.9$, consistent with $n = -17/4$ predicted for isotropic turbulence. Based on this decay rate, the maximum dissipation at 1-m depth is estimated as $\varepsilon_{max} \approx 0.2$ m^2 s^{-3}. The equivalent Hinze scale of air bubbles $a_H \approx 2$ mm is consistent with previously reported bubbles sizes in whitecaps.

An important result is the finding of increased turbulence levels beneath the forward face of the wave, up to a quarter wave period prior to the air entrainment. We find the occurrence and magnitude of the prebreaking turbulence consistent with wave–turbulence interaction of rotational waves (Thais and Magnaudet 1996), possibly initiated by microbreakers.

The average dissipation profile, including breaking and nonbreaking waves, shows a strong increase above the mean waterline, $\varepsilon(z) \propto z^{2.3}$, and nearly constant values in the trough region. The integral dissipation in the crest region is more than 2 times the dissipation in the trough region. Previous mooring and tower-based turbulence measurements were limited to the water column beneath the trough line and thus were not able to resolve the highly turbulent wave region in the crests.

Our results provide indications of the way in which turbulence models of the upper-ocean boundary layer should be modified, especially with respect to the model origin, so as to better represent the vertical structure of near-surface turbulence and its link to wave breaking.

Acknowledgments. This work was made possible with the help of the technical staff of the acoustical oceanography group at the Institute of Ocean Science; S. Vagle played an important role in designing the experiment and was, together with N. Hall-Patch, involved in the data collection. We are indebted to the crew of R/P *FLIP* and A. Jessup and J. Edson for supplementary data. The office of Naval Research provided financial support as part of the FAIRS projects.

APPENDIX

Residual Wave Orbital Motion

Although the float supporting the velocity profilers is tracking the surface oscillations, the observed velocities contain a residual signal of the wave orbital motion due to the strong depth dependence of the orbital motion. For a linear gravity wave the maximum residual vertical velocity at depth z is $\Delta w(z) = a\omega(e^{-k|z|} - e^{-k|z_F|})$, where a is the amplitude and ω is the frequency of an individual wave component and z_F is the mean penetration depth of the surface flotation. This residual velocity has a strong dependence on the wavenumber. For our setup, with $Z_F = -0.1$ m, the largest velocities are expected for about 10-m wavelength (Fig. A1a) and reach $\approx$0.15 m s^{-1}. This compares well to the observed maximum velocities (Fig. A1b). The theoretical maximum difference of the residual velocity along the profile is ~0.06 m s^{-1}. This is also in good agreement with the observed differences of mean velocities of the first five and last five velocity bins of each profile (Fig. A1b). More important, the wavenumber of any residual orbital motion is much smaller than the wavenumbers in the inertial subrange. Therefore, the wave orbital motion does not affect the dissipation estimates.

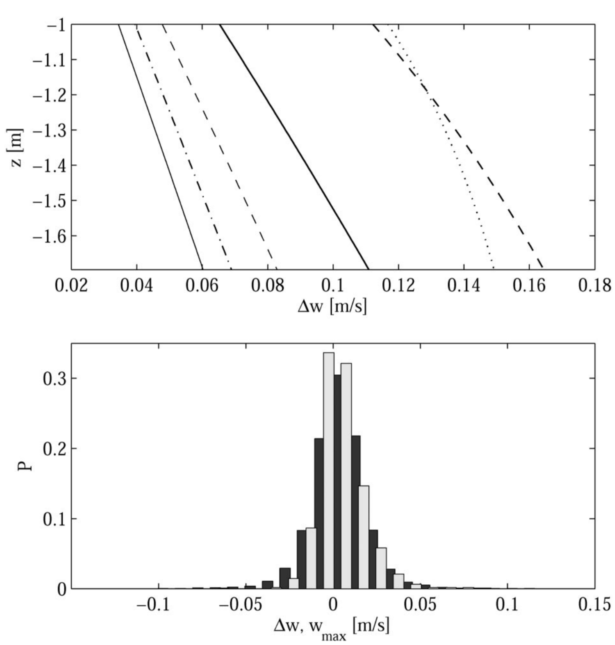

FIG. A1. (top) Simulated maximum residual orbital vertical velocity for constant wave slope $ak = 0.07$ and various wavelengths, $\lambda = 5$ (dots), 10 (thick dashes), 50 (thick solid line), 100 (thin dashes), 150 (dash–dots), and 200 m (thin solid line). (bottom) Distribution of observed maximum vertical velocities (black) and observed maximum velocity differences within each profile (gray), for deployment I.

REFERENCES

Agrawal, Y. C., E. A. Terray, M. A. Donelan, P. A. Hwang, A. J. Williams III, W. M. Drennan, K. K. Kahma, and S. A. Kitaigorodskii, 1992: Enhanced dissipation of kinetic energy beneath surface waves. *Nature,* **359,** 219–220.

Anis, A., and J. N. Moum, 1992: The superadiabatic surface layer of the ocean during convection. *J. Phys. Oceanogr,* **22,** 1221–1227.

——, and ——, 1995: Surface wave–turbulence interactions: Scaling $\varepsilon(z)$ near the sea surface. *J. Phys. Oceanogr,* **25,** 2025–2045.

Banner, M. L., J. R. Gemmrich, and D. M. Farmer, 2002: Multiscale measurements of ocean wave breaking probability. *J. Phys. Oceanogr.,* **32,** 3364–3375.

Burchard, H., 2001: Simulating the wave-enhanced layer under breaking surface waves with two-equation turbulence models. *J. Phys. Oceanogr.,* **31,** 3133–3145.

Craig, P. D., and M. L. Banner, 1994: Modeling wave-enhanced turbulence in the ocean surface layer. *J. Phys. Oceanogr.,* **24,** 2546–2559.

Deane, G. B., and M. D. Stokes, 2002: Scale dependence of bubble creation mechanisms in breaking waves. *Nature,* **418,** 839–844.

Drennan, W. M., K. K. Kahma, E. A. Terray, M. A. Donelan, and S. A. Kitaigorodskii, 1991: Observations of the enhancement of kinetic energy dissipation beneath breaking wind waves. *IUTAM Symposium on Breaking Waves*, M. L. Banner and R. H. J. Grimshaw, Eds., Springer-Verlag, 95–101.

——, M. A. Donelan, E. A. Terray, and K. B. Katsaros, 1996: Oceanic turbulence measurements in SWADE. *J. Phys. Oceanogr.,* **26,** 808–815.

Duncan, J. D., 2001: Spilling breakers. *Annu. Rev. Fluid Mech.,* **33,** 517–547.

Farmer, D. M., S. Vagle, and A. D. Booth, 1998: A free-flooding acoustical resonator for measurement of bubble size distribution. *J. Atmos. Oceanic Technol.,* **15,** 1132–1146.

Garrett, C., M. Li, and D. M. Farmer, 2000: The connection between bubble size spectra and energy dissipation rates in the upper ocean. *J. Phys. Oceanogr.,* **30,** 2163–2171.

Gemmrich, J. R., 2000: Temperature anomalies beneath breaking waves and the decay of wave-induced turbulence. *J. Geophys. Res.,* **105,** 8727–8736.

——, and D. M. Farmer, 1999a: Near-surface turbulence and thermal structure in a wind-driven sea. *J. Phys. Oceanogr.,* **29,** 480–499.

——, and ——, 1999b: Observations of the scale and occurrence of breaking surface waves. *J. Phys. Oceanogr.,* **29,** 2595–2606.

——, T. D. Mudge, and V. D. Polonichko, 1994: On the energy input form wind to surface waves. *J. Phys. Oceanogr.,* **24,** 2413–2417.

Greenan B. J. W., N. S. Oakey, and F. W. Dobson, 2001: Estimates of dissipation in the ocean mixed layer using a quasi-horizontal microstructure profile. *J. Phys. Oceanogr.,* **31,** 992–1004.

Hinze, J. O., 1975: *Turbulence.* 2d ed. McGraw-Hill, 790 pp.

Huang, N. E., Z. Shen, S. R. Long, M. C. Wu, Q. Zheng, N.-C. Yen, C. C. Tung, and H. H. Liu, 1998: The empirical mode decomposition and the Hilbert spectrum for nonlinear and nonstationary time series analysis. *Proc. Roy. Soc. London,* **454A,** 903–955.

——, ——, and ——, 1999: A new view of nonlinear water waves: The Hilbert spectrum. *Annu. Rev. Fluid Mech.,* **31,** 417–517.

Lamarre, E., and W. K. Melville, 1994: Void-fraction measurements and sound-speed fields in bubble plumes generated by breaking waves. *J. Acoust. Soc. Amer.,* **95,** 1317–1328.

Lueck, R. G., F. Wolk, and H. Yamazaki, 2002: Oceanic velocity microstructure measurements in the 20th century *J. Oceanogr.,* **58,** 153–174.

Lumley, J. L., and E. A. Terray, 1983: Kinematics of turbulence converted by a random wave field. *J. Phys. Oceanogr.,* **13,** 2000–2007.

Melville, W. K., 1996: The role of surface-wave breaking in air–sea interaction. *Annu. Rev. Fluid Mech.,* **26,** 279–321.

——, and P. Matusov, 2002: Distribution of breaking waves at the ocean surface. *Nature,* **417,** 58–52.

——, F. Veron, and C. J. White, 2002: The velocity field under breaking waves: Coherent structure and turbulence. *J. Fluid Mech.,* **454,** 203–233.

Oakey, N., 1985: Statistics of mixing parameters in the upper ocean during JASIN phases 2. *J. Phys. Oceanogr.,* **15,** 1662–1675.

Ruddick, B., A. Anis, and K. Thompson, 2000: Maximum likelihood spectral fitting: The Batchelor spectrum. *J. Atmos. Oceanic Technol.,* **17,** 1541–1555.

Siddiqui, M. H. K., M. R. Loewen, C. Richardson, W. F. Asher, and A. T. Jessup, 2001: Simultaneous particle image velocimetry and infrared imagery of microscale breaking waves. *Phys. Fluids,* **13,** 1891–1903.

Soloviev, A., and R. Lukas, 2003: Observation of wave-enhanced turbulence in the near-surface layer of the ocean during TOGA COARE. *Deep-Sea Res.,* **50,** 371–395.

——, N. V. Vershinsky, and V. A. Bezverchnii, 1988: Small-scale turbulence measurements in the surface layer of the ocean. *Deep-Sea Res.,* **35,** 1859–1874.

——, R. Lukas, P. Hacker, M. Backer, H. Schoeberlein, and A. Arjannikov, 1999: A near-surface microstructure system used during TOGA COARE: Part II. *J. Atmos. Oceanic Technol.,* **16,** 1598–1618.

Stewart, R. W., and H. L. Grant, 1962: Determining the rate of dissipation of turbulent energy near the surface in the presence of waves. *J. Geophys. Res.,* **67,** 3176–3180.

Teixeira, M. A. C., and S. Belcher, 2002: On the distortion of turbulence by a progressive surface wave. *J. Fluid Mech.,* **458,** 229–267.

Terray E. A., M. A. Donelan, Y. C. Agrawal, W. M. Drennan, K. K. Kahma, A. J. Williams III, P. A. Hwang, and S. A. Kitaigorodskii, 1996: Estimates of kinetic energy dissipation under breaking waves. *J. Phys. Oceanogr.,* **26,** 792–807.

——, W. M. Drennan, and M. A. Donelan, 1999: The vertical structure of shear and dissipation in the ocean surface layer. *The Wind-Driven Air–Sea Interface: Electromagnetic and Acoustic Sensing, Wave Dynamics and Turbulent Fluxes,* M. L. Banner, Ed., School of Mathematics, University of New South Wales, 239–245.

Thais, L., and J. Magnaudet, 1996: Turbulent structure beneath surface gravity waves sheared by the wind. *J. Fluid Mech.,* **328,** 313–344.

Thorpe, S. A., 1995: Dynamical processes of transfer at the sea surface. *Progress in Oceanography,* Vol. 35, Pergamon, 315–352.

——, T. R. Osborn, J. F. E. Jackson, A. J. Hall, and R. G. Lueck, 2003: Measurements of turbulence in the upper-ocean mixing layer using Autosub. *J. Phys. Oceanogr.,* **33,** 122–145.

Trevorrow, M. V., 1994: Measurement of ocean wave directional spectra using Doppler side-scan sonar arrays. *J. Atmos. Oceanic Technol.,* **12,** 603–616.

Umlauf, L., and H. Burchard, 2003: A generic length-scale equation for geophysical turbulence models. *J. Mar. Res.,* **61,** 235–265.

Veron, F., and W. K. Melville, 1999: Pulse-to-pulse coherent Doppler measurements of waves and turbulence. *J. Atmos. Oceanic Technol.,* **16,** 1580–1597.

Wu, J., 1992: Individual characteristics of whitecaps and volumetric description of bubbles. *IEEE J. Oceanic Eng.,* **17,** 150–158.

Zedel, L., A. E. Hay, R. Cabrera, and A. Lohrmann, 1996: Performance of a single-beam pulse-to-pulse coherent Doppler profiler. *IEEE J. Oceanic Eng.,* **21,** 290–297.